**Citation**
Vo, N.H. and Pham, T.M. and Hao, H. and Bi, K. and Chen, W. and Ha, N.S. 2022. Blast resistant enhancement of meta-panels using multiple types of resonators. International Journal of Mechanical Sciences. 215: ARTN 106965. http://doi.org/10.1016/j.ijmecsci.2021.106965

# Blast Resistant Enhancement of Meta-panels Using Multiple Types of Resonators

Nhi H. Vo[1], Thong M. Pham[2], Hong Hao[3], Kaiming Bi[4], Wensu Chen[5] , and Ngoc San Ha[6]

## Abstract

A new design is proposed for the meta-panel that consists of three components including two thin face-sheets bonded to meta-truss cores to enhance its blast resistance and energy absorption capacity. The meta-truss core comprising solid inclusions with coated soft layers exhibits exceptional wave-filtering properties by activating the local vibration of the inclusions, leading to the negative effective mass and stiffness of the meta-truss core in the corresponding frequency bandgaps, hence reducing the wave propagations. When frequencies of the applied loading fall within the bandgaps, the loading effects are not able to be transferred or significantly mitigated by the meta-truss core. In this study, the result from a previous theoretical derivation of wave propagation in an idealized meta-truss bar is used to validate the numerical model. Then, analyses of the meta-truss core configurations, e.g. the inclusion arrangement and inclusion shape on its bandgap regions and the transient responses of the meta-panel are carried out with the verified numerical model. It is revealed that a complete wave

[1] PhD Scholar, Center for Infrastructural Monitoring and Protection, School of Civil and Mechanical Engineering, Curtin University, Kent Street, Bentley, WA 6102, Australia. Email: hoangnhi.vo@postgrad.curtin.edu.au

[2] Senior Lecturer, Center for Infrastructural Monitoring and Protection, School of Civil and Mechanical Engineering, Curtin University, Kent Street, Bentley, WA 6102, Australia (Corresponding author). Email: thong.pham@curtin.edu.au

[3] John Curtin Distinguished Professor, Center for Infrastructural Monitoring and Protection, School of Civil and Mechanical Engineering, Curtin University, Kent Street, Bentley, WA 6102, Australia (Corresponding author). Email: hong.hao@curtin.edu.au

[4] Associate Professor, Center for Infrastructural Monitoring and Protection, School of Civil and Mechanical Engineering, Curtin University, Kent Street, Bentley, WA 6102, Australia. Email: Kaiming.bi@curtin.edu.au

[5] Senior Lecturer, Center for Infrastructural Monitoring and Protection, School of Civil and Mechanical Engineering, Curtin University, Kent Street, Bentley, WA 6102, Australia. Email: wensu.chen@curtin.edu.au

[6] Research Fellow, Center for Infrastructural Monitoring and Protection, School of Civil and Mechanical Engineering, Curtin University, Kent Street, Bentley, WA 6102, Australia. Email: San.Ha@curtin.edu.au

attenuation design can be achieved by utilizing properly tailored arrangements of inclusions, leading to a significantly improved protective effectiveness of the panel against blast loading. The results present a base for the optimal design of the meta-panel for structural protections against blast loading.

**Keywords**: Meta-structure; Meta-panel; Protective structures; Bandgap region; Stress wave mitigation; Blast-resistance.

## 1. Introduction

Increased terrorist activities and unexpected accidental explosions in recent years have caused catastrophic consequences and imposed great threats to public security and the economy worldwide. Ever-increasing demands to protect engineering structures used for both civil and military applications have led to the development of sandwich panels functioning as sacrificial claddings [1-4]. Sandwich panels consisting of two thin face-sheets and low-density cores are widely utilized as energy absorbers due to their superiority in stiffness-to-weight ratio and crashworthiness [5-9]. By installing on the surface of the protected structures, the role of the traditional panels is to absorb energy through plastic deformation and reduce the load transmission to the structure behind the cladding, thus protecting the main structures [9, 10].

The wide variety of sandwich structures stems largely from the diversity of sandwich core topologies and the variation of the component materials. While many different topologies of the cladding core including honeycomb [11, 12], auxetic structures [13, 14], corrugated [15, 16], and bio-inspired [17-23] have been intensively studied, sandwich core materials also range widely from stochastic cellular materials (i.e. metallic [24-27] and polymeric foams [28, 29]) to periodic lattice materials [30, 31]. Specifically, metallic lattice structures have been proposed with various topologies such as pyramidal [32, 33], tetrahedral [34, 35], and hollow truss lattice [34, 36]. The dynamic performance of sandwich structures having metallic lattice cores has been investigated extensively, both experimentally and theoretically. For instance, Liu et al. [37] performed experimental and numerical investigations of the responses of hollow cylinders with metallic foam core panels subjected to air blast. The simulation results well captured the deformation patterns of the sandwich panels observed in the tests. For applications under impact and blast loads, investigations on the transient responses of sandwich panels have shown great energy absorption capacity compared to the monolithic panel as sacrificial claddings [38, 39].

Recent attention has been directed to the field of locally resonant meta-structures [40-43], which are the hybrid of metamaterial-based concepts with optimal lattice topology. It is worth mentioning that the prefix “meta” originates from the Greek preposition, which meant “beyond”, implying these exotic structural behaviours are superior to other natural counterparts. These novel engineering structures are expected to possess the ability to generate exceptional wave propagation mitigations in frequency ranges called “bandgap” [44, 45], leading to unique wave attenuation properties not found in nature [46-49]. Such properties are activated due to the presence of specially designed man-made structures [43]. A bandgap is a frequency band in which incoming waves cannot propagate due to the activation of local resonance within the inclusions [40, 50]. Potential practical applications in engineering fields by generating favourable bandgaps of these structures including dynamic load mitigation [51, 52], vibration control [53, 54], sound isolation [55], and seismic isolation [56, 57], etc. Multiple techniques have been employed to explore the unique characteristics of these structures. For instance, a local resonant structure that utilizes steel balls coated with silicone and covered in an epoxy cube was proposed by Liu et al. [58], which demonstrated that when the frequency of the excitation force is close to the local resonance frequency, the effective mass becomes negative. This unusual property originates from the interaction between the propagating waves and the resonance of the steel balls. For instance, Li et al. [43] proposed meta-lattice sandwich panels with single-resonators, which show the blast attenuation and high energy absorption owing to the local resonance of the internal resonator with soft coatings. They also carried out experimental investigations on the wave-filtering characteristics of the meta-lattice truss for validation [59]. It was demonstrated that the performance of the meta-panels is superior to that of the solid counterparts with the same mass due to the coupled mechanism of absorbing strain energy through both plastic deformation and local resonance. Subsequently, to enhance the dynamic performance of the meta-panel against blast loads by broadening its bandgap regions,

the dual-meta panel was proposed [42]. The theoretical results showed that a dual-meta panel has wider bandgaps than those with single-resonators, indicating it can filter wave energy in wider frequency ranges and thus has higher protection efficiency. However, despite all these recent works on mitigation wave propagation, the relevant research on the effectiveness of the meta-panel on structural protection against impact and blast loading, especially blast loading, is still very limited. Therefore, further study of the meta-truss core to achieve the most effective dynamic loading mitigation performance of meta-panels for structural protection is needed.

This study systematically performs numerical investigations on the behaviours of meta-panel subjected to blast loading and proposes the new design of the meta-panel with multiple types of meta-cores as a sacrificial cladding against blast loading (see Fig. 1). To validate the accuracy of the numerical model, the meta-truss bar used to form the meta-panel is firstly modelled numerically. The theoretically derived results of an idealized meta-truss bar in a previous study are used to verify the numerical model in terms of the bandgap regions and transmission coefficient. The verified model is utilized to build the numerical model of the meta-panel and perform a series of parametric studies to investigate the influences of the inclusion arrangement and inclusion shape on the effectiveness of the meta-panel on wave propagation mitigation. The best performing designs are identified to maximize the blast-resistant performance of the meta-panels. In-depth discussions on the influences of critical parameters on the bandgap regions and the dynamic behaviours of the meta-panel are also given. This study numerically and analytically demonstrates the dynamic mitigation mechanism of the proposed meta-panel under blast loads. The obtained results provide interesting findings which can be used for various engineering applications.

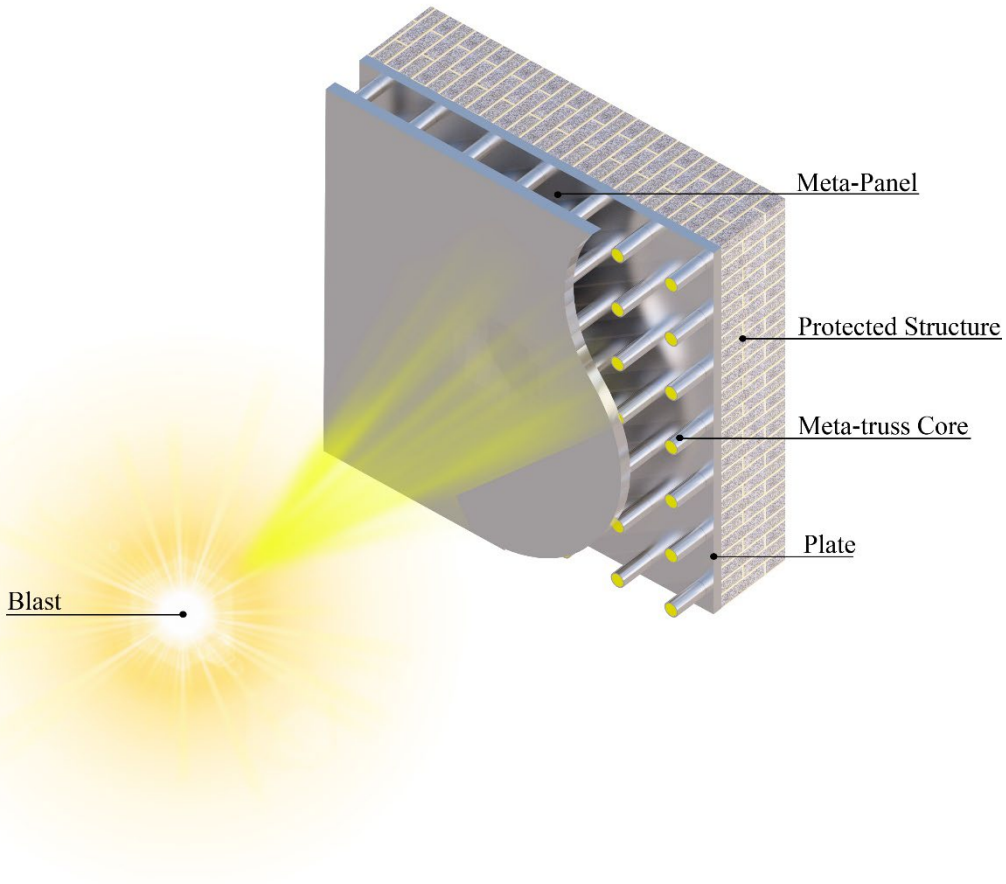


Fig. 1. Schematic diagram of the meta-panel consisting of two plates and meta-truss cores functions as a sacrificial cladding to protect the main structure against blast loading.

## 2. Meta-panel configurations

The configurations of the meta-panel shown in Fig. 2 (a) consists of two identical aluminium face-sheets with the dimension of 120 mm x 120 mm and the meta-truss cores. The meta-truss bar with resonators (see Fig. 2(b)) considered in this study comprises 6 modules in which each module (shown in Fig. 2 (c)) has three components including the outer tube, soft coating, and resonators. While the tube and resonators are made of aluminium, polyurethane (PU) which can experience large plastic deformation is selected for the soft coating. It should be noted that tungsten is also used to make resonators in the parametric analysis in this study to investigate the influences of resonator core materials on meta-panel properties. The dimensions and

materials are chosen to preserve the bandgap-generating behaviours at large strain for the meta-panel, which is important for structures under extreme loading threats. Also, its structural design could be tailored to adapt to different loadings by adjusting geometrical parameters. The influences of different parameters will be compared in Section 5.2. All material properties used in the numerical model in this study are listed in Table 1.

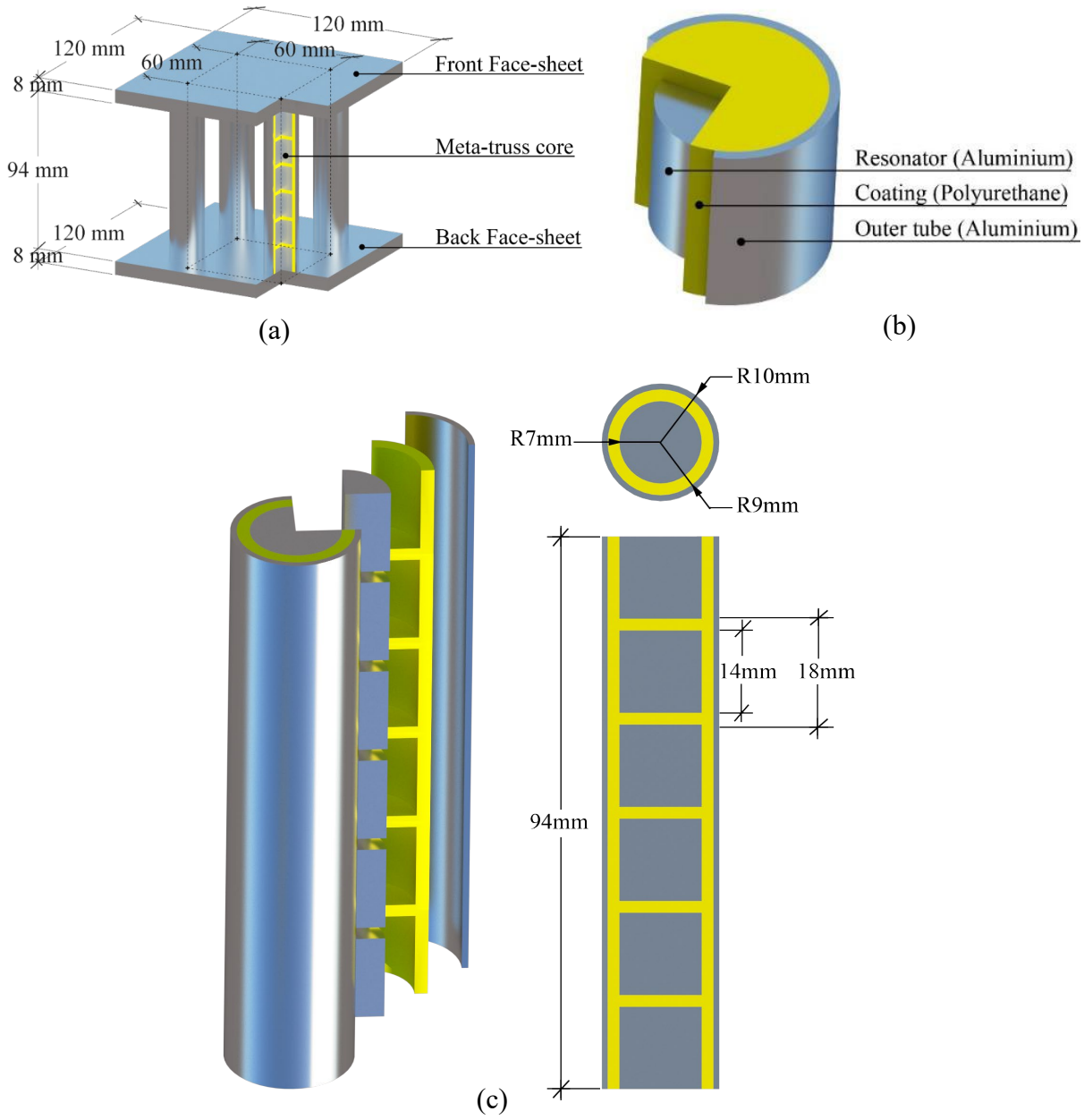


Fig. 2. Design of meta-panel (a) Schematic view of the meta-panel with a partial view cut to display the embedded meta-cores, (b) a module constituent forming the meta-truss bar

includes the outer tube, the coating and the resonators, and c) meta-truss bar is made of 6 modules and its sectional dimension.

Table 1. Material properties of the meta-panel [43]

| Materials | Material properties | | |
|---|---|---|---|
| | Density $\rho$ (kg/m$^3$) | Young's modulus $E$ (GPa) | Poisson's ratio $v$ |
| Aluminium | 2,770 | 70 | 0.33 |
| Polyurethane | 900 | 0.147 | 0.42 |
| Tungsten | 19,300 | 411 | 0.28 |

## 3. Programmable negative properties

To quantify the bandgap regions of the meta-truss bar induced by the resonant feature of the meta-core, the dynamic effective mass $m_{eff}$ and effective stiffness $k_{eff}$ using a one-dimensional spring-mass model with internal resonators can be expressed as follows [60]:

$$m_{eff} = m_1 - \frac{k_2}{\omega^2} \tag{1}$$

$$k_{eff} = k_1 - \frac{1}{4}\left(m_1 - \frac{k_2}{\omega^2}\right)\omega^2 \tag{2}$$

in which $m_1$ is the mass of the resonator in the spring-mass model as shown in Fig. 3, $k_1$ and $k_2$ respectively represent the axial spring and the shear spring of the soft coating while the angular frequency is denoted by $\omega$. As seen from Fig. 4, the dynamic effective mass becomes negative in the frequency range of 0 kHz to 9.1 kHz and then gradually increases to positive values. Whereas in the frequency range of 23.2 kHz to 50 kHz, the effective stiffness is negative. It is worth mentioning that the interested frequency range in this study is only up to 50 kHz, covering the frequency band of common blast loads acting on structures [61]. The associated frequency regions where $m_{eff}$ and $k_{eff}$ become negative are termed as the 1$^{st}$ bandgap and the 2$^{nd}$ bandgap,

respectively. The resonators move out-of-phase against each other, leading to wave propagation mitigation in the bandgap. The incident wave within these frequency ranges can be significantly mitigated due to the energy being transferred and stored in the relative motions of the resonators.

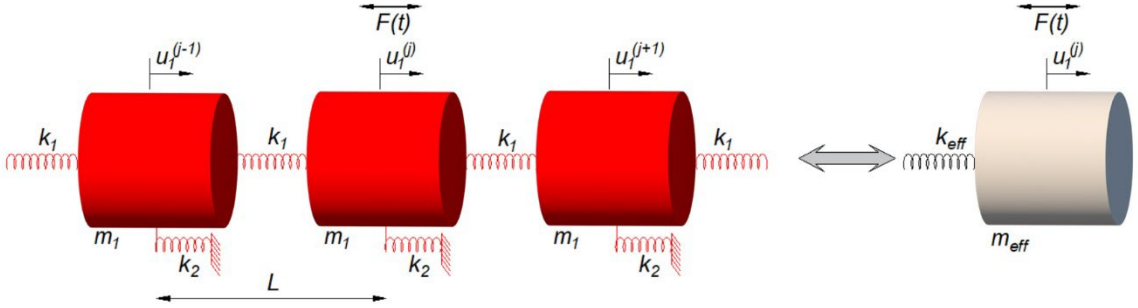


Fig. 3. The simplified spring-mass model including mass $m_1$, axial stiffness $k_1$ and shear stiffness $k_2$ with respect to the continuum media and its equivalent effective model with effective mass $m_{eff}$ and effective stiffness $k_{eff}$.

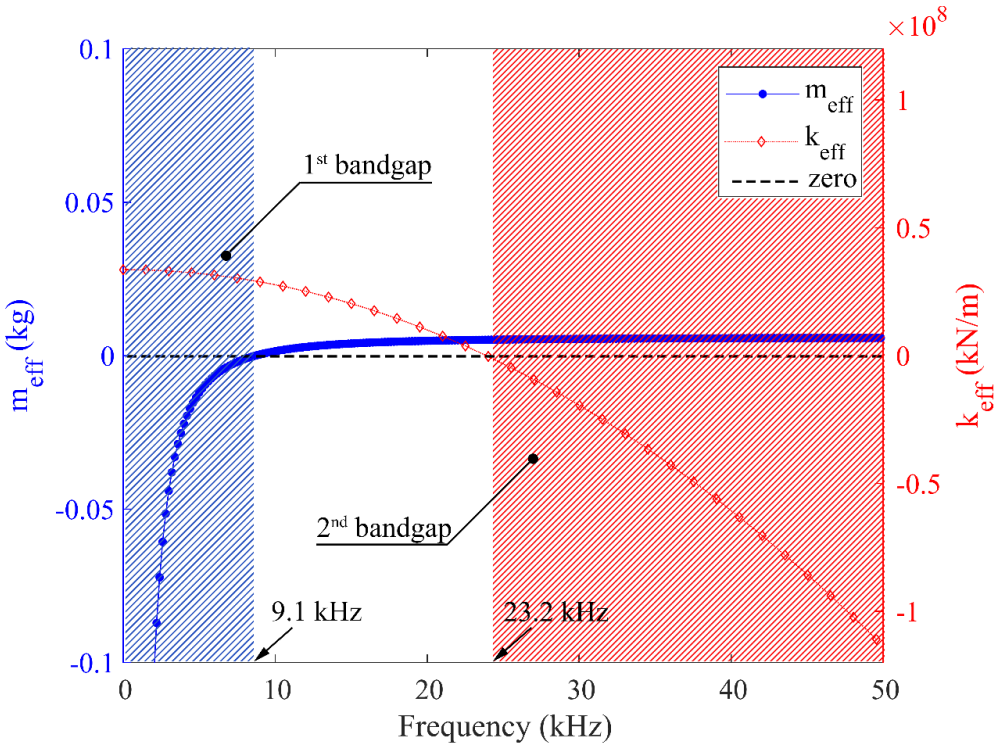

Fig. 4. Effective parameters of the spring-mass model to show the theoretical bandgap regions of the meta-truss bar including the effective mass on the left-hand side and the effective stiffness on the right-hand side. Shaded areas in blue and red indicate the bandgaps associated with the negativity of the effective mass and effective stiffness, respectively (For interpretation of the references to colour in this figure legend, readers are referred to the web version of this article).

The transmission of energy of the entire system can be quantified by using the transmission coefficients, $T$, which can be computed as follows:

$$T = \left| \prod_{j=1}^{N} \frac{u^{(j)}}{u^{(j-1)}} \right| = \prod_{j=1}^{N} T^{(j)} \tag{3}$$

where $u^{(j)}$ is the displacement of the $j^{\text{th}}$ unit cell, and $N$ is the total number of the unit cells.

## 4. Blasting wave characteristics

Determining the dominant frequencies of the applied loading is the vital step for the engineering design of the meta-panel. It is because the negativity of the effective parameters is only triggered when the applied loading frequency falls into the bandgap region of the meta-panel, leading to its favourable mitigation performance. In this study, the blast load is applied on the front face-sheet of the meta-panel. The keyword *LOAD_BLAST_ENHANCED is widely utilized in LS-DYNA to generate blast load via the Conventional Weapon Effects (CONWEP) program, which predicts the air blast load based on empirical data from blasting tests. This model was also adopted in the Unified Facilities Criteria (UFC 3-340-02) in graphical form for designing structures to resist the effects of the explosion. The loading area definition is determined by the keyword *LOAD_BLAST_SEGMENT whereas the function *DATABASE_BINARY_ BLSTFOR is utilized to compute the blast pressure. The blast

pressure on the meta-panel is calculated by the equivalent amount of Trinitrotoluene (TNT), the stand-off distance, and the angle of incidence. The blast pressure is predicted as follows [62]:

$$P(t) = P_r cos^2\theta + P_i(1 + cos^2\theta - 2cos\theta) \quad (4)$$

where $P_i$ and $P_r$ are respectively the incident pressure and reflected pressure while $\theta$ denotes the angle of incidence. Computation of $P_i$ and $P_r$ is based on the scaled distance, $Z = R/\sqrt[3]{W}$, in which $R$ and $W$ are the stand-off distance and the equivalent amount of TNT, respectively [63]. In this study, the blast charge TNT is placed perpendicularly to the centre of the front face-sheet at a distance of 0.35 m, in which the angle of incidence $\theta$ is defined as 0. The size of the charge is 0.4 kg which corresponds to the scaled distance of 0.41 m/kg$^{1/3}$. Fig. 5 (a) shows the reflected pressure time-history of the blast loading. To obtain the corresponding frequency spectrum, the blast time history is converted to the frequency domain by utilizing the Fast Fourier Transform (FFT) method, the FFT spectrum of the blast load is shown in Fig. 5 (b). As shown, the peak reflected pressure is approximately 36 MPa and the dominant blast loading energy distributes in the frequency band up to 50 kHz.

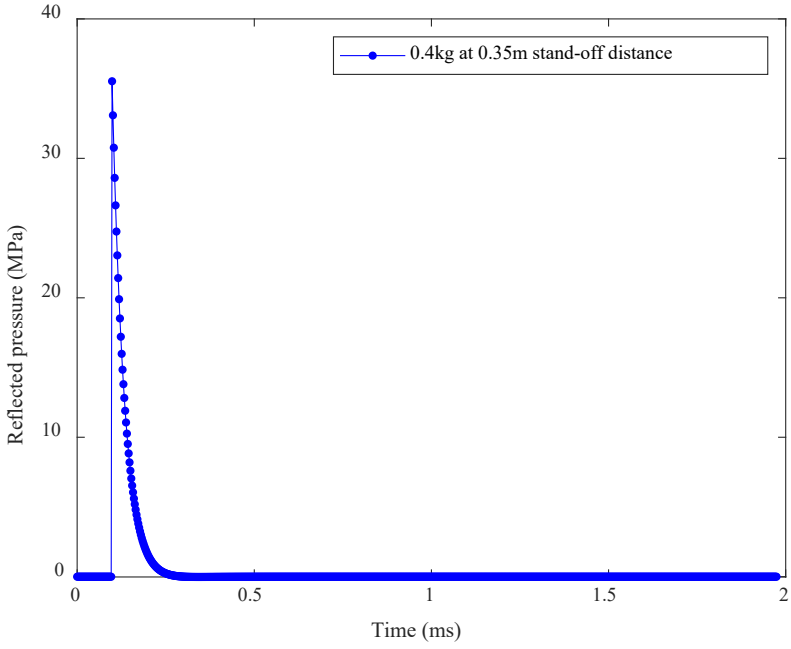


(a)

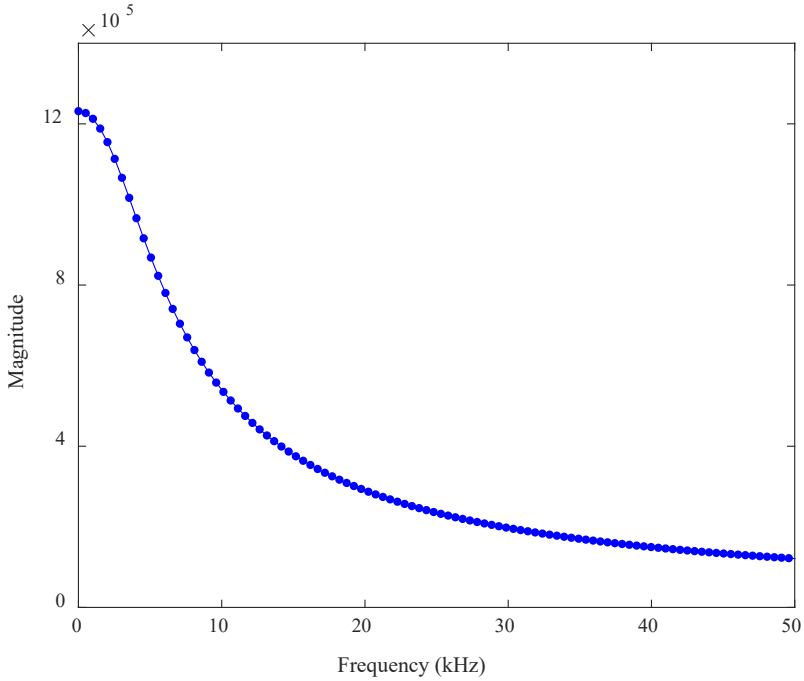


(b)

Fig. 5. Peak reflected pressure profile of the simulated blast loading generated by 0.4 kg TNT at 0.35m stand-off distance (a-b) in time history and its FFT spectrum.

## 5. Comprehensive numerical investigations

The complete bandgap of the meta-truss bar generated by the arrangement of multiple resonators is proposed in the present model and its effect on the dynamic performance of the meta-panel is analysed in this section. The influence of the inclusion geometry on the transient response of the meta-panel is also numerically investigated for various shapes. In addition, the model validation is carried out to check the accuracy of the simulations in this section.

### 5.1 Model development and verification

The theoretical solution has been used to calculate the bandgap regions of the meta-truss bar based on the one-dimensional spring-mass model. Due to the complexity, the infinite number of modules and single harmonic wave input have been assumed to analytically solve the Eigen frequencies and calculate the bandgap regions. It is not straightforward to derive the closed-form theoretical solutions of the complex case considering the finite number of modules,

boundary reflections, and various input loading conditions. In addition, the structural responses of the meta-panel subjected to blast loading are more challenging to obtain analytically when considering plastic deformation. To overcome the limitations mentioned above, numerical simulations are performed to investigate the bandgap regions and the transient responses of the meta-panel subjected to blast loadings. The results obtained from the above theoretical solutions based on idealized conditions are utilized to verify the accuracy of the numerical simulations.

In this study, commercial software LS-DYNA is utilized to evaluate the bandgap regions of the meta-truss bar (Fig. 2c)) and the dynamic behaviours of the meta-panel (Fig. 2(a)). As illustrated in Fig. 6, the entire meta-panel is modelled. In the simulation, all elements are meshed by the solid hexahedron elements with a minimum mesh size of 1 mm after performing a mesh convergence analysis. The interfaces between the inclusions and polyurethane are modelled by the kinematic constraint method in which the selected segments are tied to each other and assumed to be perfectly bonded. This contact is chosen to prevent the slide or detachment between the meta-cores and the soft coating which is of significance to activate the local resonance of the resonators. To obtain rigid connections, the contact between the outer truss bar and the two face-sheets is also defined by the kinematic constraint method while the interior contact between layers of interior surfaces of polyurethane is adopted to eliminate the negative volume issue which often occurs due to large deformation of soft materials. In addition, all nodes along the face-sheet edges are assumed to be constrained in all three directions, which account for the peripherally clamped boundary of the back face-sheet. The material properties used in LS-DYNA are listed in Tables 1-2.

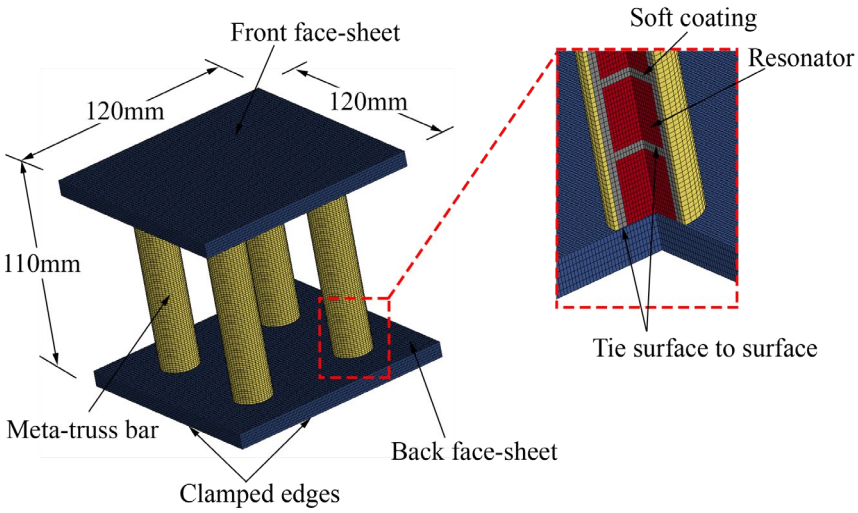


Fig. 6. Schematic of the finite element model used to investigate the dynamic response of the meta-panel. The meta-panel is peripherally clamped at the back face-sheet and all contact definition in the model is simulated by tied surface to surface.

187 Table 2. Johnson-Cook material parameters for aluminium [43]

| Density ($kg/m^3$) | Poisson's ratio | Young's Modulus (GPa) | A (Pa) | B (Pa) | C | m | n | $T_m$ (K) | $T_r$ (K) | $\dot{\varepsilon}_0$ (1/s) |
|---|---|---|---|---|---|---|---|---|---|---|
| 2770 | 0.33 | 70 | 0.369 | 0.675 | 0.007 | 1.5 | 0.7 | 800 | 293 | 1.0 |

188 To verify the developed numerical model, the derived theoretical analysis of the transmission
189 coefficient of a single truss bar obtained by Eq. (3) is calculated to compare with the
190 corresponding numerical results. A meta-truss bar consisting of 6 unit cells as shown in Fig.
191 2(c) is numerically built. The input signal is applied at one end of the meta-truss bar by a sweep
192 frequency ranging from 0 – 50 kHz while the output signal is captured at the other opposite
193 end. It should be noted that the clamped boundary condition is adopted on the peripheral edges
194 of the truss bar to represent the practical boundary condition in reality. The numerical
195 transmission coefficient of the meta-truss bar displayed in Fig. 7 agrees closely with the
196 analytical result, indicating the validity of the model. In particular, it is depicted in Fig. 6 that

197 the meta-truss bar possesses two bandgaps in the frequency ranges of [0 – 9.1] kHz for the 1st
198 bandgap and [23.2 – 50] kHz for the 2nd bandgap while the corresponding ranges from the
199 numerical result are [0 – 9.3] kHz and [22.5 – 50] kHz. There is a slight bandgap disagreement
200 between the two approaches and oscillations of the numerical results. This is because the
201 infinite number of unit cores is assumed in the analytical derivation, while the numerical meta-
202 truss bar has a finite length with 6 unit cores. In addition, each unit core is numerically modelled
203 with its respective elastic material property and density instead of the lumped mass connected
204 with idealized lumped springs in the analytical solution.

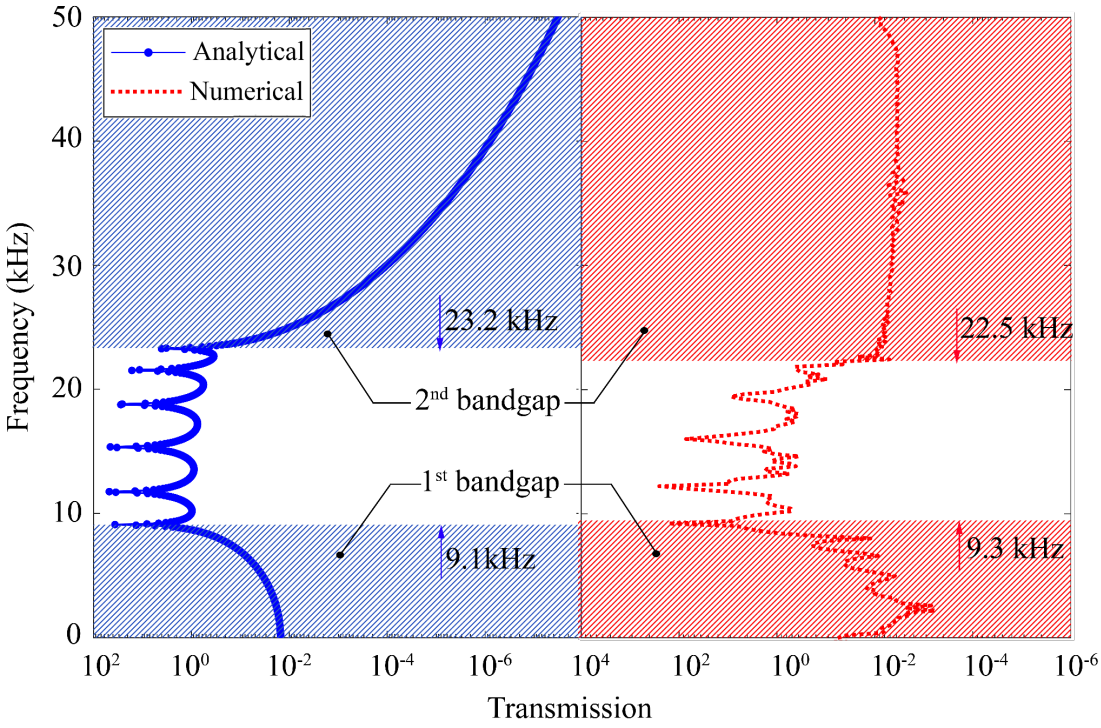


Fig. 7. Comparison of the transmission coefficients of the meta-truss bar including the analytical solution on the left-hand side and the numerical result on the right-hand side. Shaded areas in blue colour indicate the theoretical bandgaps while the corresponding numerical predictions are shown in red shaded areas (For interpretation of the references to colour in this figure legend, readers are referred to the web version of this article).

For further validation, a prescribed displacement u(t) with the amplitude of $10^{-4}$ (m) and multi-frequency components including $f_1$ = 5 kHz, $f_2$ = 16 kHz, and $f_2$ = 30 kHz, $[i.e., u(t) = 10^{-4}(sin[2\pi \times 5t] + sin[2\pi \times 16t] + sin[2\pi \times 30t])$, is applied to the input end of the meta-truss bar and the output end is set free. Fig. 8 shows the displacement-time histories at the two ends of the meta-truss bar (i.e. the input and the output, respectively) and the corresponding FFT spectra. As observed, waves attenuation is observed as expected with only one input signal of 16 kHz passing through the meta-truss bar while other signals of 5 kHz and 30 kHz, which fall in its bandgap are eliminated. This demonstrates that the meta-truss bar possesses the wave filtering capacity at the frequencies falling in its two bandgaps. Generally, the numerical models and analytical predictions are well matched. The numerical model in predicting the bandgaps and wave attenuations of the meta-truss bar is verified, which is extended to model the meta-truss panel for the investigation of its blast mitigating performance.

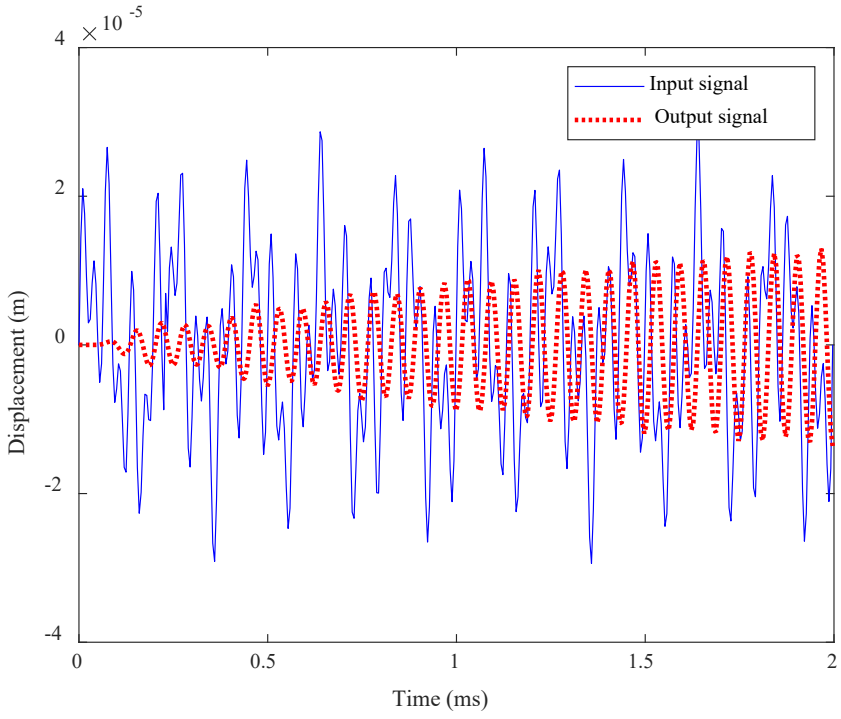


(a)

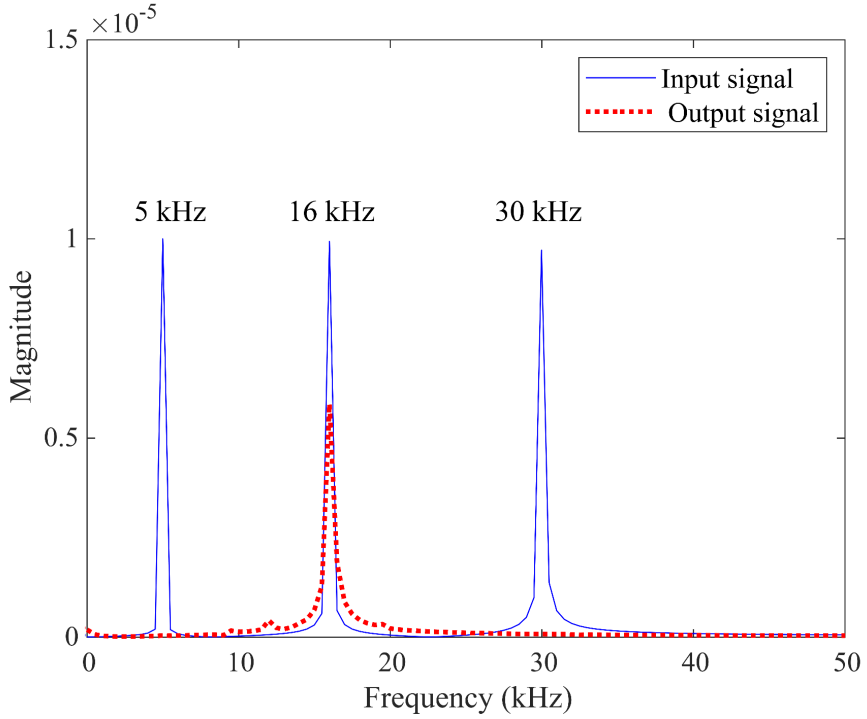


(b)

Fig. 8. Input prescribed displacement is excited at one end of the meta-truss bar while the output displacement is captured at the other end. The displacements of the input and output respectively denoted by the blue solid line and red dotted line are illustrated in (a) time histories and (b) FFT spectra.

## 5.2 Parametric studies

The meta-panel was found to possess superior blast mitigation capacity and outperforms other conventional counterparts, e.g. sandwich panels with hollow trusses and solid trusses under blast loading [42]. To obtain the favourable design of the meta-panel, systematic parametric studies with the aims of maximizing the bandgaps of the meta-truss cores and thus its blast-resistant performance are conducted in this section. Inclusion arrangements and inclusion shapes are selected as parameters for investigation because with their appropriate design, the better wave attenuation of the meta-truss bar and the enhanced performance of the meta-panel can be achieved. The blast loading described in Section 4 is applied to all considered panels

while the description of the meta-panel in Section 2 is referred as the reference. To evaluate the blast mitigation capacities, the critical criteria such as peak force transmitted to the protected structure, energy absorption, the central displacement of the back face-sheet are compared among the panels with different core configurations. These particular criteria are chosen due to the main functionality of the meta-panel as a sacrificial cladding is to absorb energies from the incident loadings, therefore, minimizing force transmissions to the protected structures. Besides, the central displacement is measured to determine the response amplitude and damage of the meta-panels subjected to blast loading.

### 5.2.1 *Influence of inclusion arrangement*

In this section, the meta-panel with multiple types of resonators is modelled. Under blast loading, its blast-resistant performances are expected to enhance as compared to the meta-panel with uniform resonators, because of the complete bandgap created by its arrangement that covers the entire targeted frequency band with most blast loading energy. For comparison, the dynamic responses of the meta-panels with traditionally uniform resonators are also evaluated.

#### 5.2.1.1 Influence of multiple types of meta-cores

While travelling through a meta-truss bar, stress waves can either propagate in the passband or be attenuated in the bandgaps depending on the frequency of the applied loading. A uniform arrangement of identical resonators, i.e., meta-cores, limits the width of the bandgaps to a narrow frequency range. To overcome this limitation and intensify the performance of the meta-core, instead of utilizing the same repetitive units, the meta-truss bar with multiple types of meta-cores is proposed to maximize the width of the bandgap and minimize the corresponding passband. It should be noted that the materials and dimensions of the face-sheets and outer tube of the meta-truss bar remain unchanged. This proposed meta-truss bar (Fig. 9a) composes of two zones, denoted by Zone 1 and Zone 2. Each zone has uniform unit cells with the same

geometry, but different resonators made of tungsten (W) and aluminium (Al), with their properties given in Table 1.

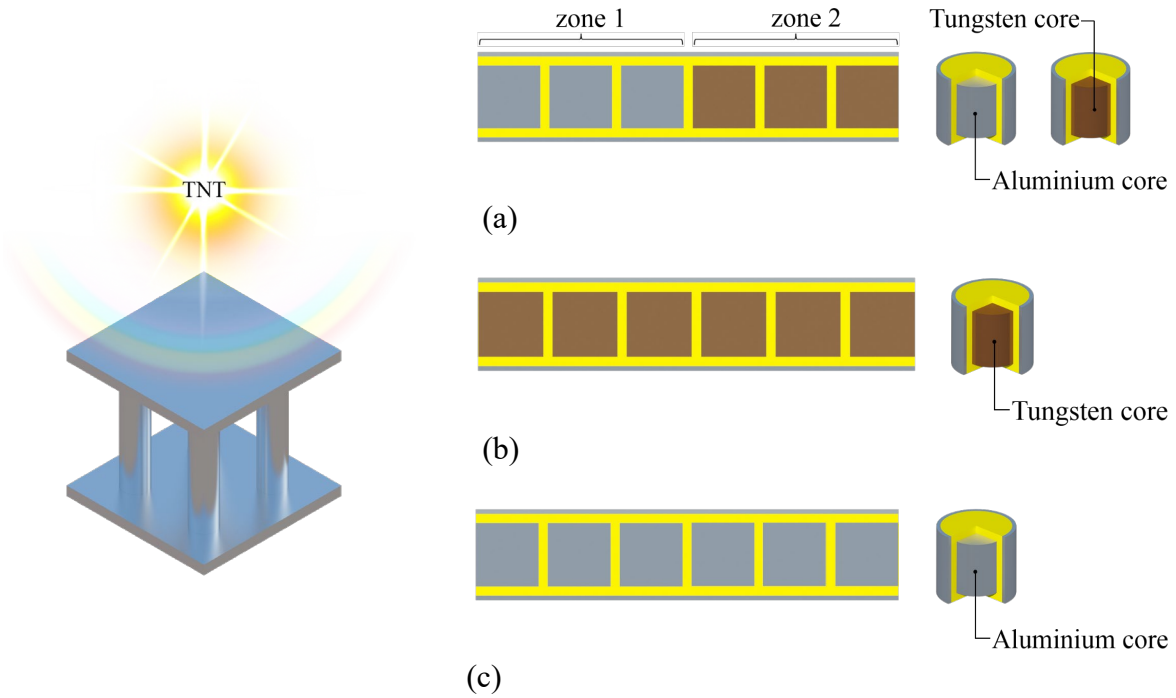


Fig. 9. Schematic diagrams of the meta-panel subjected to blast loading and the meta-truss bars with different arrangements of resonators: meta-truss bars with (a) 3 Aluminium cores and 3 Tungsten cores, (b) 6 Tungsten cores and (c) 6 Aluminium cores.

Fig. 10 illustrates the analytical transmission coefficient of two zones of the meta-truss bar. The bandgap of Zone 1 corresponding to the aluminium meta-truss core is divided into a low ($LB_1$) and a high ($HB_1$) sub-band while its passband is denoted by $PB_1$. In the frequency band structure [64], which is an interval in the frequency domain comprising the bandgap and the passband [65], $HB_1$ exhibits negative effective stiffness whilst the negativity of effective mass is reflected by $LB_1$. Similarly, the passband of Zone 2 ($PB_2$) corresponding to the meta-truss bar with tungsten core lies between the first and second attenuation bands which are denoted by $LB_2$ and $HB_2$, respectively. In theory, it is practically impossible to eliminate the passband utilizing a uniform arrangement of the resonator due to the existence of the passband. Given these properties, the combination of two or more zones with different resonator cores in each zone in a meta-truss bar makes it possible to minimize or even eliminate the passband if the passband

of one zone falls into the bandgap of another zone, and vice versa. In other words, the passbands $PB_1$ and $PB_2$ can be eliminated by combining two different zones in its structural arrangements. Fig. 10 shows the elimination of both passbands PB1 and PB2 using the proposed structural combination. Specifically, $PB_2$ falls into the low bandgap of Zone 1 ($LB_1$), while the high attenuation band of Zone 2 ($HB_2$) covers all the passbands of zone 1 ($PB_1$). This finding agrees with those reported in the literature on locally resonant acoustic meta-material [66]. From the theoretical point of view, a properly programmable arrangement of resonators can maximize the bandgap width of the meta-truss bar to cover all the loading frequency bands. It means that all the incident waves can be completely stopped by the proposed meta-truss bar. Therefore, the meta-truss bar can be properly designed with multiple types of resonators to have their combined bandgaps cover the entire or as much as possible the frequency band of the input dynamic loadings for best mitigation of loading effects, hence the most effective structural protections.

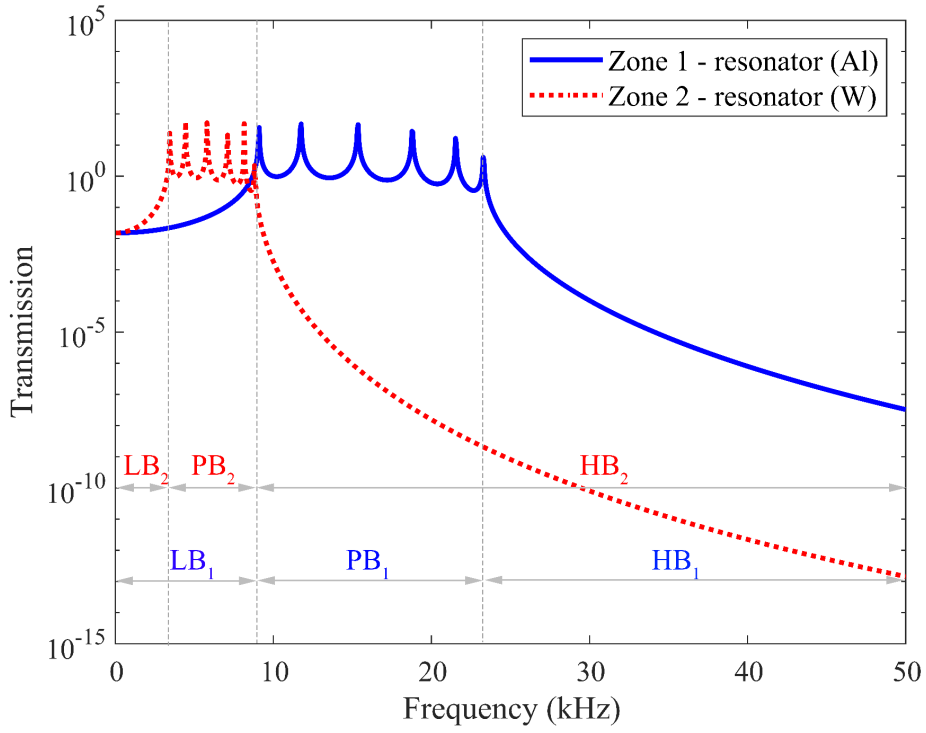

Fig. 10. Analytical transmission coefficient profile of two zones of the meta-truss bar incorporating two types of resonators (Aluminium and Tungsten). The passband $PB_2$ falls into the low bandgap of Zone 1 ($LB_1$), while the high bandgap of Zone 2 ($HB_2$) covers the passbands of zone 1 ($PB_1$). The complete bandgap is formed by combining all the four bandgaps.

The physical meaning and mechanism of wave attenuation can be well understood by observing wave propagation through the meta-truss bar with two types of resonators. To demonstrate this, a prescribed displacement consisting of three sinusoidal waves with the same amplitude but different frequencies, $i.e. u(t) = 10^{-4}(sin[2\pi t] + sin[2\pi \times 4t] + sin[2\pi \times 12t])$ is used as input to the truss bar. It is worth noting that the frequencies are chosen in such a way that each zone attenuates different frequencies. Fig. 11 shows the longitudinal displacement profile at different points in the central axis of the meta-truss bar denoted by A, B, and C. These displacements represent the input signal, response at the end of Zone 1, and response at the end of Zone 2, respectively. As shown, the peak value of the displacement is sequentially reduced by each zone of the meta-truss bar, and two zones with different resonators can attenuate the three harmonics, therefore only very low values of displacement are present at the end of the meta-truss bar. This result agrees with the previous findings on locally resonant acoustic meta-material from Comi and Driemeier [66]. In general, the newly proposed configuration with multiple types of resonators proves to be more efficient for wave filtering.

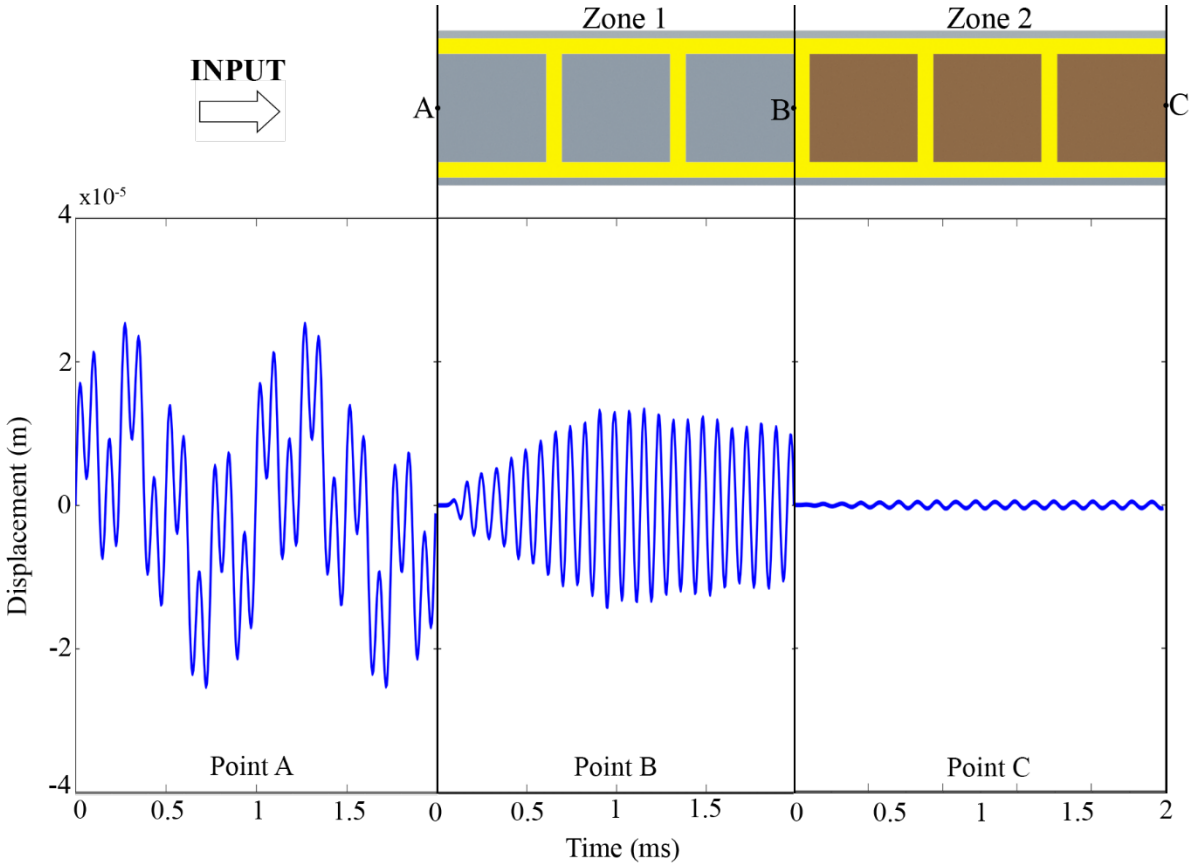


Fig. 11. Displacement-time history at three points, i.e. the input point (A), the middle point (B), and the output point (C) in the meta-truss bar with two types of resonators. A prescribed displacement excitation is applied at one end of the meta-truss bar (A), the output displacements at the middle point (B) and the ending point (C) are presented to prove the mitigation effectiveness.

To further clarify this effect, the responses at three different locations (one for each lattice zone), are shown in the frequency domain in Fig. 12. After propagating through Zone 1 (point B), only the frequencies of 1 kHz and 4 kHz are attenuated, therefore, the response has one peak at 12 kHz which falls into the passband of Zone 1. The second region of the considered meta-truss bar (Zone 2) continues attenuating the wave energy at the frequency of 12 kHz because it falls into the bandgap of Zone 2, leading to the complete attenuation of the input wave by the meta-truss bar at point C. It is noted that a small amount of energy is still transmitted as indicated by a small peak at 12 kHz in the signal after propagating through the meta-truss bar. This is because

when the core starts vibrating inside the unit cell, the initial out-of-phase vibration greatly attenuates the wave energy transmission through the unit. The reverse vibration of the core, however, still results in a small amount of wave energy transmission. Using more meta-units would further reduce the wave energy that could be transmitted through the meta-truss bar.

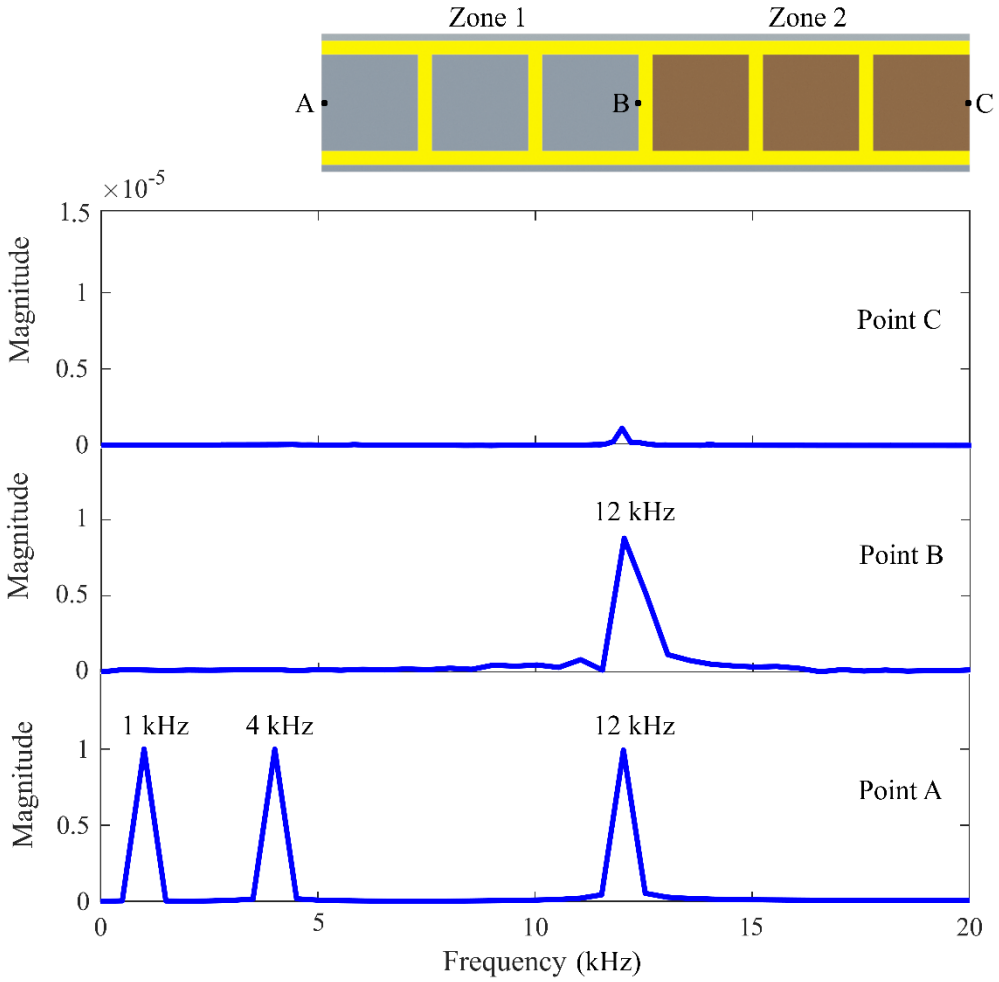


Fig. 12. FFT spectrum of displacement at the three points, i.e. the input point (A), the middle point (B), and the output point (C) in the meta-truss bar with two types of resonators. A prescribed displacement excitation is put at one end of the meta-truss bar (A), the output displacements at the middle point (B) and the ending point (C) are captured and transformed to the frequency domain.

For further demonstration, the continuous wavelet transform (CWT) [43] is adopted to analyse the wave propagation in the meta-lattice truss at three considered points in the time-frequency

domain. In this study, a Gabor wavelet transform is chosen as the mother wavelet function owing to its multiresolution analysis capability. Fig. 13 depicts the multi-frequency CWT profiles at three locations along the meta-truss bar in the case of prescribed displacement excitation with multi-frequency components. As shown, the signal energy of point A is focused at the frequencies of 1 kHz, 4 kHz, and 12 kHz (Fig. 13a) while there is very little energy exists in the output signal (point C), implying a complete wave attenuation phenomenon in these frequency bands (Fig. 13c). Besides, Fig. 13b shows the energy reduction occurs particularly at the frequencies of 1 kHz and 4 kHz, which fall into the bandgap of Zone 1. These bandgaps well agree with the analytical results as discussed above.

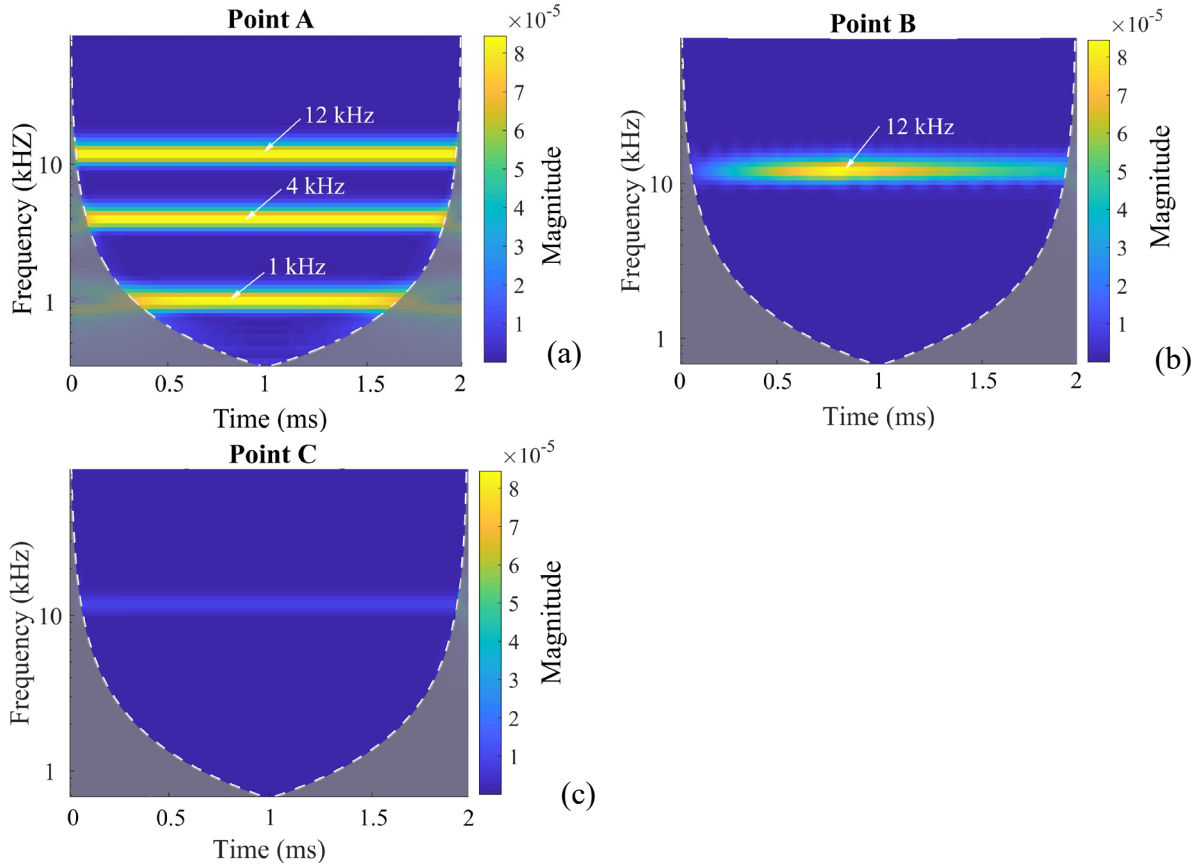


Fig. 13. Scalograms of displacement in the time-frequency domain at different points (a) point A, (b) point B, and (c) point C. A prescribed displacement excitation is put at one end of the meta-truss bar (A), the output displacements at the middle point (B) and the ending point (C) are captured and transformed to the time-frequency domain using CWT.

The design optimization analysis for the meta-panels considered in this study under blast loadings is evaluated by using combinations of multiple types of meta-cores. Structural responses (i.e. displacement of the back face-sheet and reaction force) and energy absorption capacity of the meta-panels with uniform resonators (i.e. aluminium and tungsten) and two types of resonators subjected to blast loading are compared. It is noted that the displacement is recorded at the centre of the back face-sheet in all cases, and the absolute peak values are presented wherever applicable. The blast load time history generated above as shown in Fig. 5 is used in all the analyses.

Fig. 14 shows the simulated deformation of the meta-panel and displacements on the central symmetric plane of the back face-sheet of the three meta-panels. In particular, Fig. 14(a) shows the deformation contour when the meta-panel is composed of the meta-truss bar with two types of cores, and those with the meta-truss bar having only tungsten or aluminium cores are shown in Fig. 14(b) and Fig. 14 (c), respectively. As shown, the meta-panel consisting of the meta-truss bar with two types of resonators results in the lowest value of the peak central point displacements of the back face-sheet, i.e. 2.6 mm, followed by 3.4 mm and 3.7 mm, respectively for uniform resonators of W and Al. These results indicate that using two types of meta-core together in the truss bar leads to a significant reduction of the peak response of the meta-panel as compared to the case with the uniform meta-core. This is because the combination of these two cores results in wider bandgaps of the meta-truss bar, therefore, leads to more effective stress wave propagation mitigation.


(a) two types of resonators

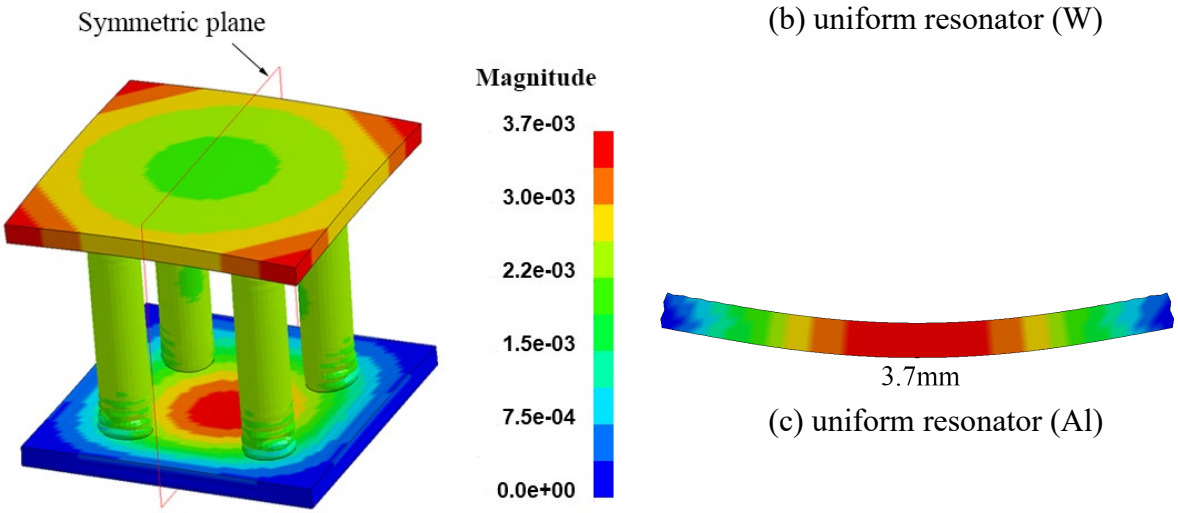


Fig. 14. Diagrams showing deformed meta-panel subjected to blast loading and the deformation on the central symmetric plane of the bottom face-sheet of three meta-panels with different meta-truss bar configurations (a) Aluminium and Tungsten resonator meta-panel and (b-c) are uniform resonator meta-panels made of tungsten and aluminium, respectively.

To further compare the dynamic response of meta-panels with different resonator arrangements, the time histories of the reaction force around the edges are shown in Fig. 15. It is observed that the peak reaction force is significantly affected by the resonator arrangements. When the two types of resonators are used in the meta-panel, it results in more reduction of the reaction force in comparison with the two meta-panels with the single type of resonators considered in the present investigation. The lowest reaction force is observed to be 140 kN in the meta-panel with the meta-truss bar consisting of two types of meta-cores, which is around 21% and 10% less than that of the panel with uniform Al and W meta-cores, respectively. This is because the meta-truss bar with two types of meta-cores has a wider frequency bandgap as demonstrated above, therefore leads to more effective stress wave mitigation, thus less stress from the blast load is transferred to the back face-sheet and then the supports.

Furthermore, to gain insight into blast response mitigation, energies absorbed by individual components, i.e. front face-sheet, back face-sheet, outer tube, and coating+core for all panels are presented in Fig. 16. It is noted that the total energy imparted from the applied blast load to the meta-panels is converted to kinetic and internal energies. While the internal energy is dissipated by inelastic deformation of the face-sheet and the outer tube, the kinetic energy is stored elastically by coating+core by their relative movements. As shown, the meta-panel with two types of meta-cores has the highest total energy absorption (i.e. 310 J), indicating its best protective effectiveness. This substantial increase in total energy absorption is mainly contributed by the rising in energy absorption by the coating+core (i.e. 33%) because by introducing two zones of resonators, the meta-core possesses a wider bandgap and filters more stress waves from the blast loading, leading to more energy absorption. As a result, the back face-sheet of the meta-panel with two types of meta-cores absorbs less energy (i.e. 14%) compared to the other two meta-panels with the single type of meta-core due to its less deformation, while the energy absorption of the front face-sheet and the outer tube remains unchanged among the three considered panels. This effectiveness is due to the energy absorption associated with the motion of the resonator masses. No such energy absorption mechanism is available for the meta-panel with uniform resonators. Among the three panels investigated, the meta-panel with two types of resonators yields the best blast effect attenuation performance due to the merging bandgap of two different zones of resonators.

Overall, the panel with the meta-truss bar composing two types of resonators possesses better blast mitigation and higher energy absorption capability compared to the uniform-resonator panel, even the panel with the meta-truss bar made of tungsten cores, which is heavier because of the higher density of tungsten than aluminium. Therefore, it is crucial to choose a proper combination of the meta-cores for the meta-panel in such a way that it results in wider bandgaps for better blast protection of structures.

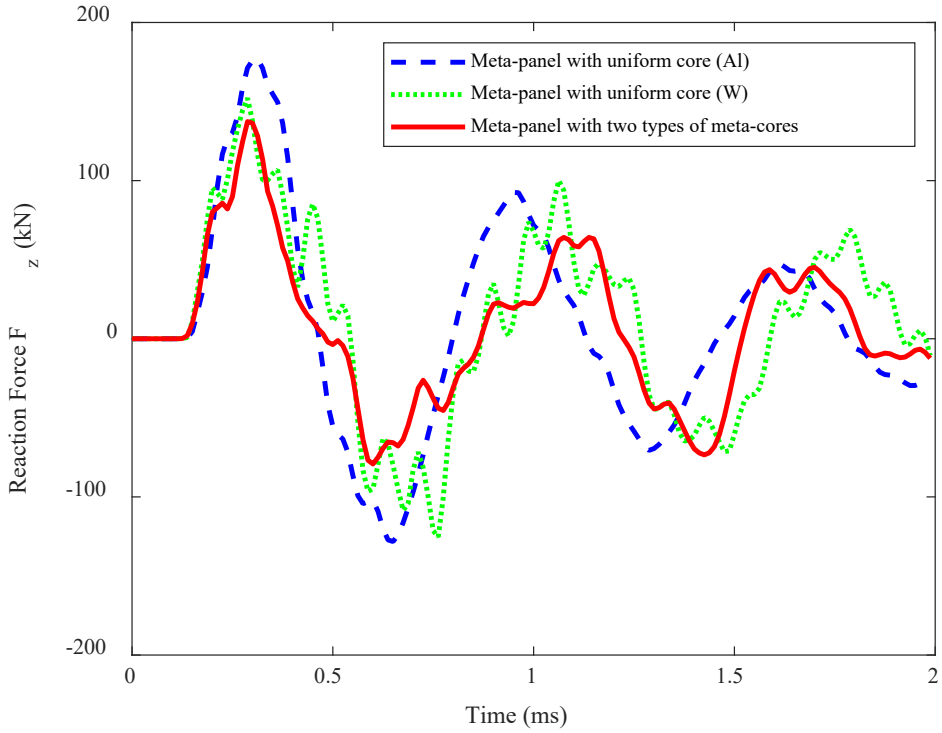


Fig. 15. Comparison of reaction force-time history curves between the three meta-panels including meta-panel with two types of resonators and conventional meta-panels with uniform resonators (Al or W) under blast loading.

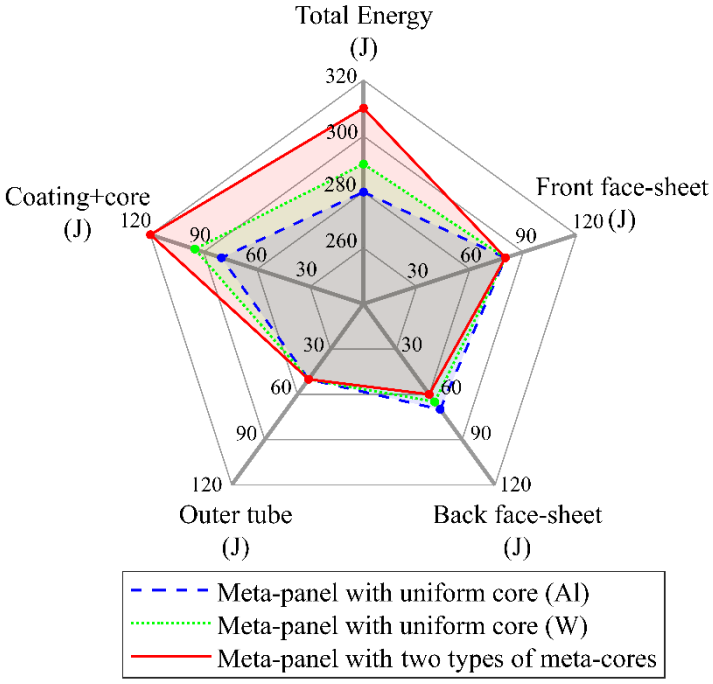

Fig. 16. Comparison of energy absorptions of different parts of the three meta-panels including meta-panel with two types of resonators and conventional meta-panel with uniform resonator (Al or W) under blast loading.

5.2.1.2 Influence of inclusion size

Besides material properties, the bandgap of the meta-core is also affected by its dimension and geometry [50]. Therefore the desired bandgap of the meta-core can also be achieved by adjusting the dimension and geometry of the core. In this section, the influences of the meta-core size on the frequency bandgaps are investigated. Fig. 17a depicts the proposed meta-truss bar which consists of two types of resonators with different radii while the meta-truss bars with uniform aluminium resonators of 7 mm and 4 mm radius are illustrated in Figs. 17b and 17c, respectively. Other parameters, namely the material properties, the diameter and the thickness of the outer tube remain unchanged in the three meta-truss bars.

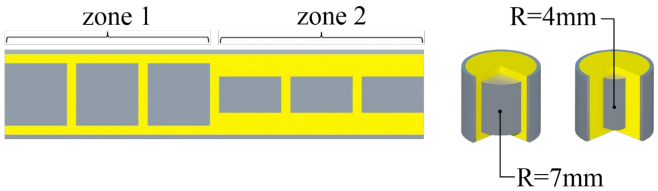


(a)

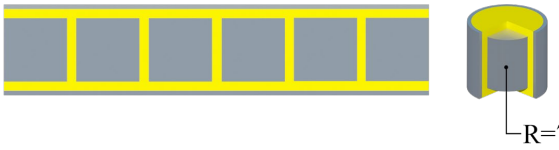


(b) meta-truss bar with uniform resonators (R=7mm)


(c) meta-truss bar with uniform resonators (R=4mm)

Fig. 17. Schematic diagram of meta-truss bars with different sizes of resonators (a) non-uniform resonator meta-truss bar with two sizes of resonators and (b-c) are uniform resonators meta-truss bar with the core radius of 7 mm and 4 mm, respectively.

Fig. 18 illustrates the bandgaps of two meta-cores of two sizes. Same as the results presented above, the frequency band structure of the individual zone consists of two bandgaps and one passband as highlighted in blue and red, respectively. It can be seen that in the bandgaps denoted by $LB_i$ and $HB_i$ (i=1,2), combining the bandgaps of these two meta-cores generates a wider bandgap covering the entire frequency band from 0 to 50 kHz. In other words, by introducing two zones of resonators with different sizes, the passband $PB_i$ in the range of 0 to 50 kHz can be eliminated, leading to complete wave attenuation. This is because that reducing the core size by introducing Zone 2 decreases the mass of the inclusion while increasing the thickness of the coating mass. As the result, the value of the mass and shear stiffness significantly decreases, resulting in a higher lower bound frequency and a broader range of the $1^{st}$ bandgap that completely covers the passband of Zone 1. As a consequence, wave energy in the frequency band of 0 to 50 kHz would be greatly mitigated by the truss bar with these two types of meta-cores.

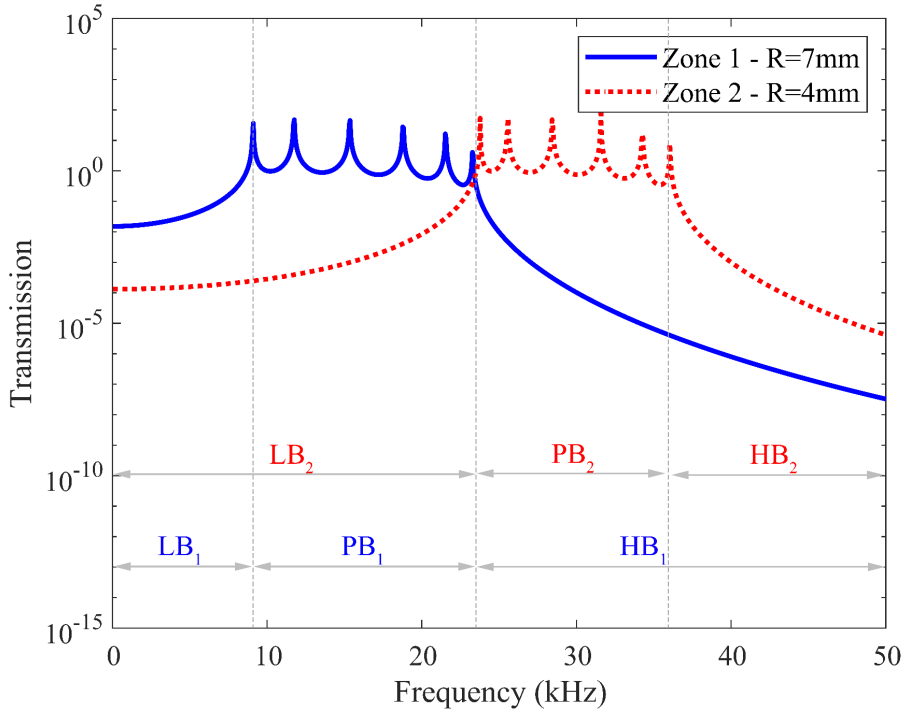


Fig. 18. Analytical transmission coefficient profile of two zones of the meta-truss bar with two types of resonators with the radii of 7 mm and 4 mm. The passband $PB_2$ falls into the low bandgap of Zone 1 ($LB_1$), while the high bandgap of Zone 2 ($HB_2$) covers the passband of zone 1 ($PB_1$). The complete bandgap is formed by combining all the bandgaps.

For clarification, a sweep excitation in the frequency range [0 – 50] kHz is applied to one end of the meta-truss bar while at the central and far ends, the vibration displacements are compared (Fig. 19). It is noted that the input displacement amplitude of the excitation is high, which decreases at the end of Zone 1 because the bandgap of Zone 1 mitigates the transmission of wave energy with the frequencies falling in its bandgap. The displacement amplitude reduces almost to zero at the end of the truss bar because the remaining wave energy has frequencies mainly inside the bandgap of Zone 2. The effectiveness of the bandgap, resulting in the mitigation of the input excitation, is demonstrated in Fig. 18, showing the response time histories at different locations of the truss bar.

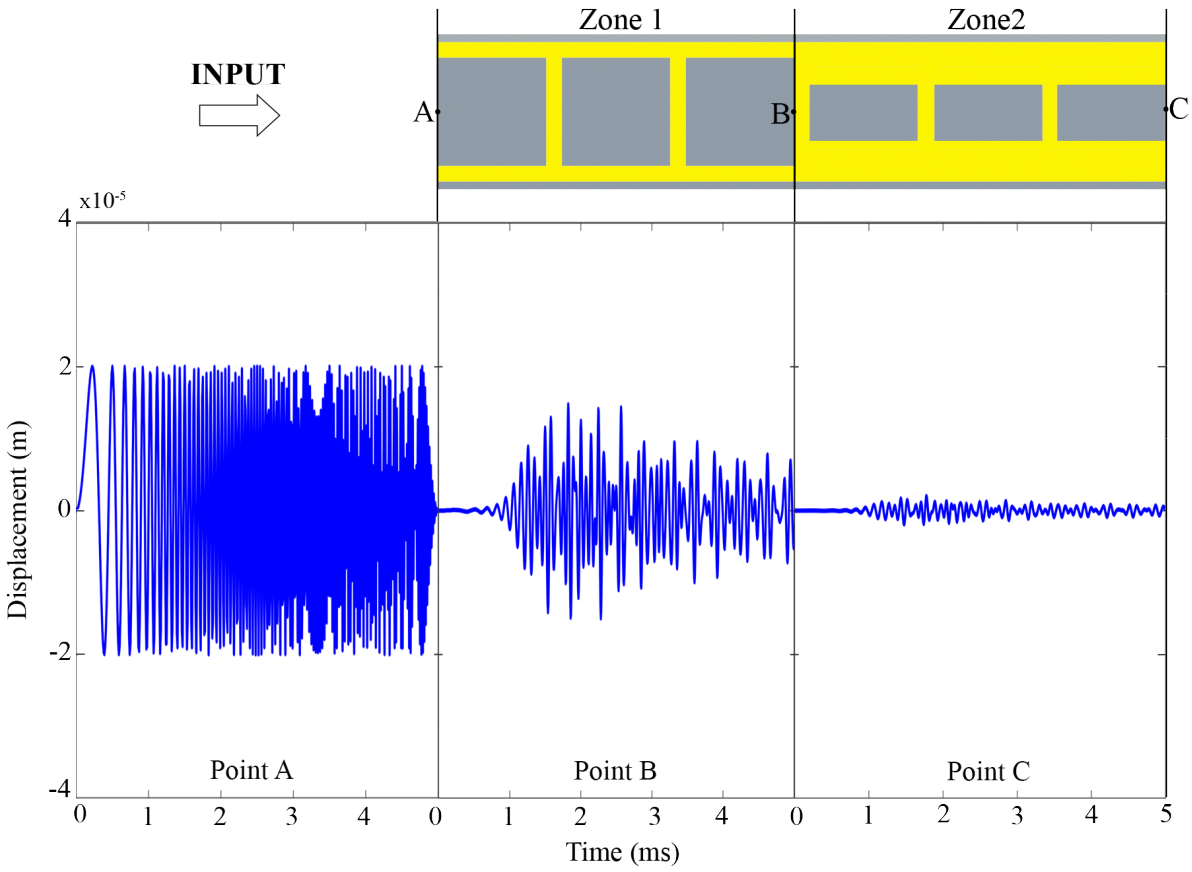


Fig. 19. Displacement-time history at the three points, i.e. the input point (A), the middle point (B), and the output point (C) in the meta-truss bar with two resonator sizes. A prescribed displacement excitation is applied at one end of the meta-truss bar (A), the output displacements at the middle point (B) and the ending point (C) are presented to prove the mitigation effectiveness.

Fig. 20 shows the FFT spectrum of the displacement time histories shown in Fig. 19. The effect of the bandgap in filtering the wave energy is obvious. As shown, at point B after wave propagating through the meta-cores in Zone 1, wave energy in the frequencies in the bandgap of 0 – 9.1 kHz and 23.2 – 50 kHz is attenuated. After further propagating through meta-cores in Zone 2, most wave energy is attenuated. Fig. 21 shows the multi-frequency CWT profiles of the time histories at three locations along the meta-truss bar shown in Fig. 19. Similar observations can be drawn again. These findings indicate that the predicted bandgaps of the

meta-cores from the analytical results exist in the meta-truss bars, which effectively mitigate wave propagations.

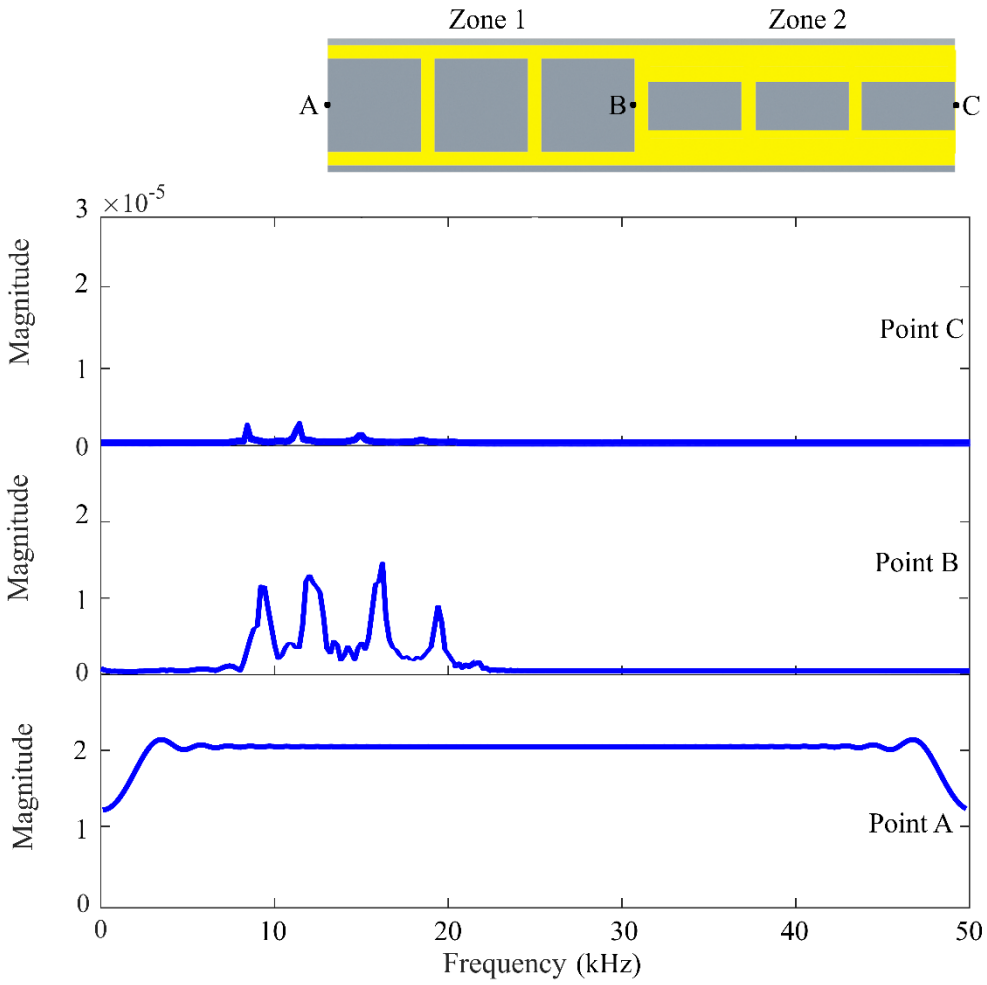


Fig. 20. FFT spectrum of displacement at the three points, i.e. the input point (A), the middle point (B), and the output point (C) in the meta-truss bar with two resonator sizes. A prescribed displacement excitation is applied at one end of the meta-truss bar (A), the output displacements at the middle point (B) and the ending point (C) are captured and transformed to the frequency domain.

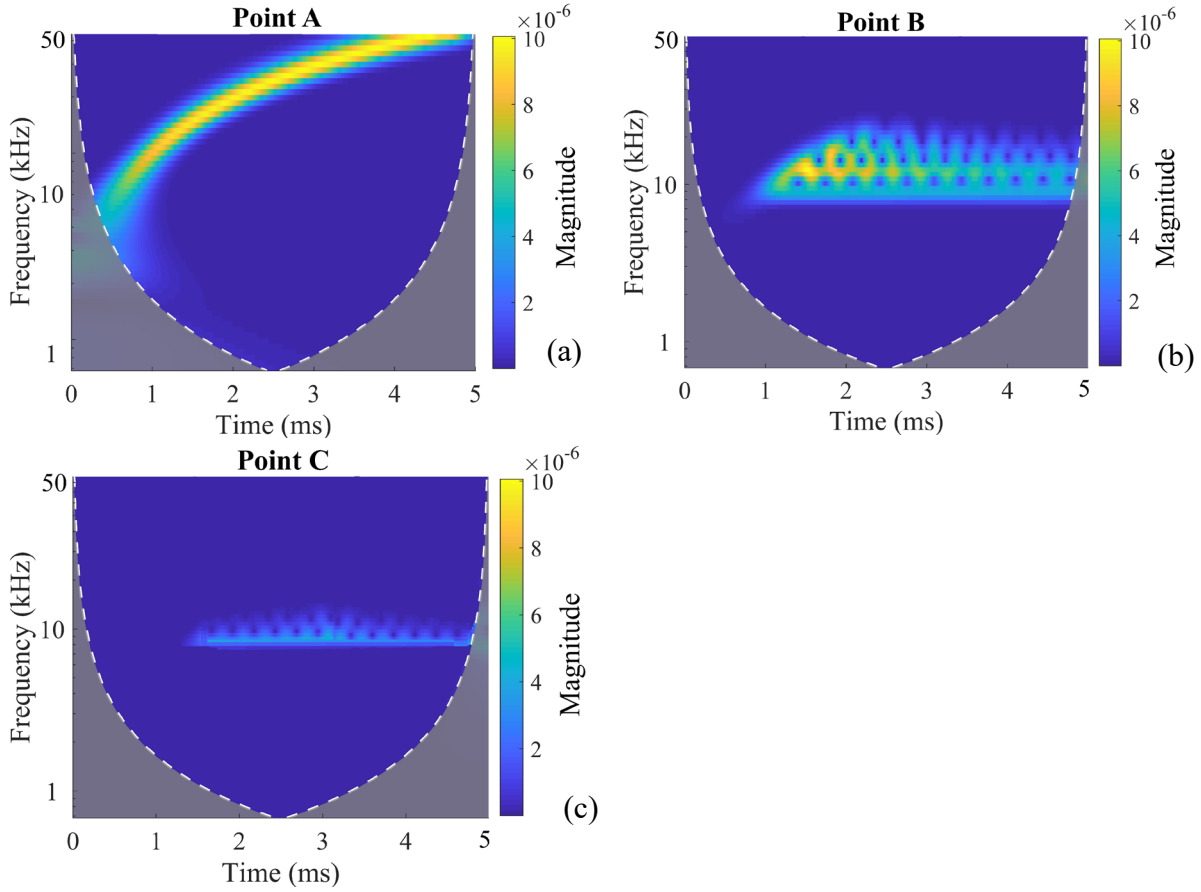


Fig. 21. Scalograms for displacement in the time-frequency domain at different points (a) point A, (b) point B, and (c) point C. A prescribed displacement excitation is applied at one end of the meta-truss bar (A), the output displacements at the middle point (B) and the ending point (C) are captured and transformed to the time-frequency domain using CWT.

Three meta-panels with the above meta-truss bars, i.e., uniform meta-cores with the radius of 7 mm and 4 mm (R7 and R4) and combined cores with both radii of 7 mm and 4 mm subjected to blast loading are considered. For illustration, the peak displacement of the back face-sheet of the meta-panels is shown in Fig. 22 while the reaction force of the panel around the edges is given in Table 3. As shown, the meta-panel consisting of two resonator zones demonstrates better performance in all criteria, with the smallest displacement of the back face-sheet, the lowest reaction force, and the highest energy absorption among the three considered meta-panels. In particular, the results show that the peak displacements at the centre point of the back

face-sheet of the panel with uniform resonator (i.e. R7 and R4) are 3.7 mm and 3.9 mm respectively, compared to 2.7 mm of the panel with meta-truss bar consisting of two sizes of cores.

As expected, the meta-panel with two types of meta-cores show a significant reduction in reaction force. The peak reaction force of 137 kN is around 22% and 28% less than that of the panel with meta-truss consisting of the uniform resonator of R7 and R4, respectively because of the wider frequency bandgap of the truss bar with combined cores than the meta-truss bar with uniform cores as discussed above. The energy absorption by "coating + core" of the meta-truss bar with non-uniform cores is also higher, which leads to smaller energy absorption by the back face-sheet of the non-uniform resonator panel, indicating smaller plastic deformation of the back face-sheet and better protection of the panel. In addition, the meta-panel with uniform resonators (R7) outperforms its peer with R4 against blast loading. This is because the bandgap becomes wider with the increased mass of the resonator [67]. Overall, the panel with the meta-truss bar composing two types of cores with wider frequency bandgaps possesses better blast mitigation and higher energy absorption capability.

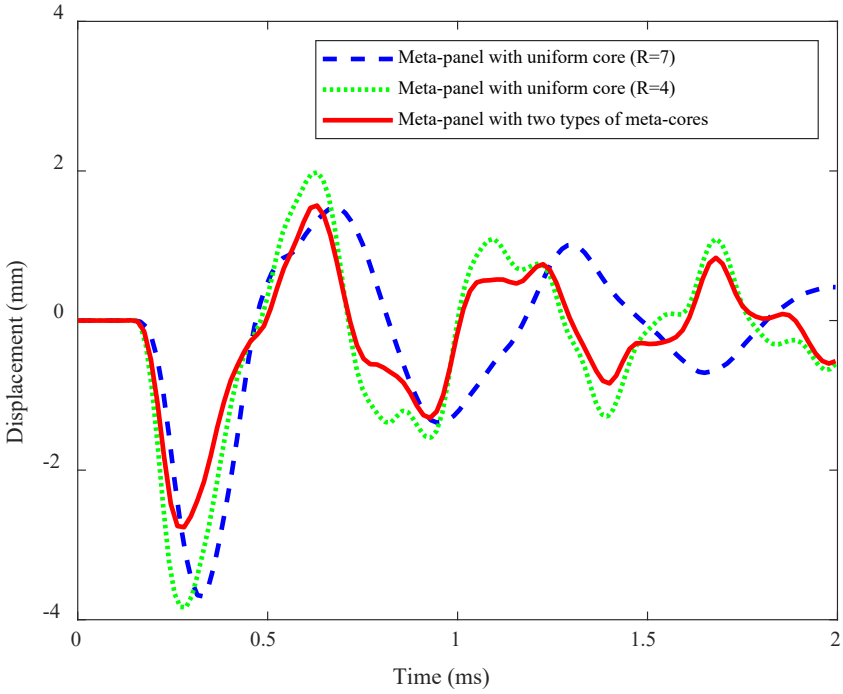


Fig. 22. Comparison of displacement-time history curves of the back face-sheet between the three meta-panels including meta-panel with two resonator sizes and conventional meta-panels with uniform resonators (7 mm or 4 mm of radius) under blast loading.

Table 3. Influence of non-uniform inclusion on reaction force and energy absorption.

| **Inclusion arrangement** | **Reaction force (kN)** | **Energy absorption (J)** | | | | |
|---|---|---|---|---|---|---|
| | **$F_z$** | **Front facesheet** | **Back facesheet** | **Truss** | **Coating + Core** | **Total** |
| Uniform (R=7 mm) | 177.5 | 80 | 70 | 50 | 80 | 280 |
| Uniform (R=4 mm) | 190.4 | 81 | 74 | 50 | 60 | 265 |
| Non-uniform | 137.0 | 79 | 61 | 50 | 120 | 310 |

5.2.2 *Influence of inclusion shapes*

Previous studies have investigated the inclusion configurations and their effects on the bandgap locations and the bandwidth of locally resonant acoustic meta-materials [67-71]. There is only limited research of this effect on the meta-truss bar and dynamic behaviours of meta-panels [69]. In this subsection, four regular shapes including cylinder, cuboid, pentagonal prism, and hexagonal prism are considered to evaluate the influence of the core geometry on the bandgap

characteristics and the transient responses of the meta-panel made of truss bars with those meta-cores. The schematic diagrams of the unit cell with various inclusion shapes of meta-truss bars embedded in the soft coating are illustrated in Fig. 23. While the inclusion shape is different, other parameters of the meta-panel (Section 2) and the blast loading (Section 4) are kept the same in this investigation. It is worth mentioning that the mass and the length of the inclusion are respectively kept constant at $5.97\times10^{-3}$ kg and 14 mm for all considered cases.

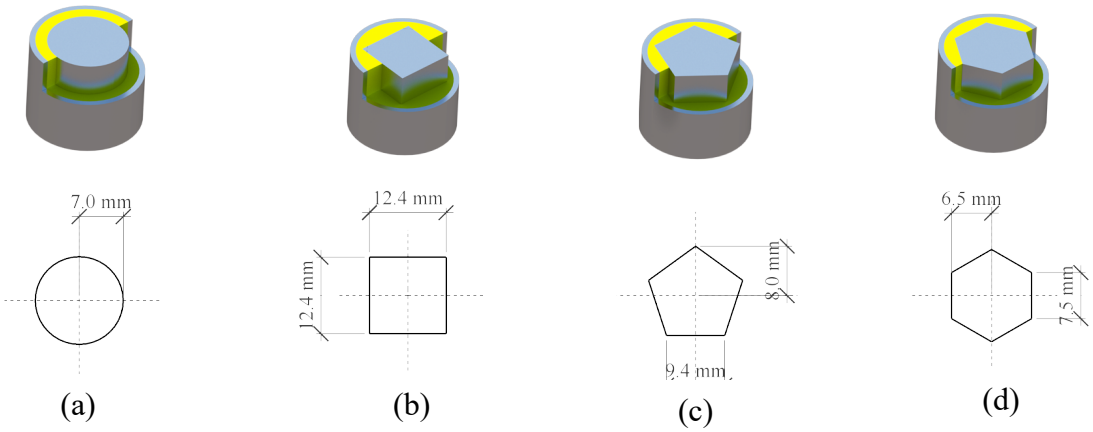


Fig. 23. Representation and dimensions of meta-unit cells with various inclusion shapes including (a) cylinder, (b) cuboid, (c) pentagonal prism, and (d) hexagonal prism.

Fig. 24 shows the frequency band structures and the percentage of blast energy in the bandgaps of the meta-truss bar with different inclusion shapes, in which the bandgap regions are shown by solid bars while dashed line and solid line denote the complete passbands and the blast loading energy in the bandgap region, respectively. It is worth mentioning that the percentage of the blast loading energy fall in the bandgap is calculated by dividing the energy falling in the bandgaps by the total blast loading energy. It can be observed that the frequency band structures change pronouncedly for different cases, indicating the effect of the shape inclusion on the bandgap regions. In Fig. 24, the lower bound and upper bound of the band structures are evaluated by solving Eqs. (1) and (2). As shown, the cuboid core generates the widest first bandgap from 0 to 10.9 kHz, while the cylinder core has a narrowest first bandgap from 0 to 9.1 kHz among the four considered core geometries. This can be attributed to the relationship

between the shear stiffness ($k_2$) which is related to the lateral surface area and the width of the 1st bandgap. It was reported that the 1st bandgap width increases with the shear stiffness [40]. Of all the considered shapes, the cuboid has the largest surface area in the transverse direction which corresponds to the largest shear stiffness.

On the other hand, there are no substantial variations regarding the 2nd bandgap width and the lower bound frequency of the 2nd bandgap by varying the inclusion shape. Therefore, the meta-truss with the cuboid core has the narrowest passband and hence the best wave mitigation capacity, as shown in Fig. 24. These results are consistent with those reported in the previous findings on locally resonant acoustic meta-material [69] and meta-concrete [67]. Specifically, cuboid inclusion could decrease the passband width from 14.1 kHz to 13 kHz as compared to the cylindrical shape. It shows that the pentagonal and hexagonal prism inclusions generate the narrower passband width by 0.7 kHz and 0.2 kHz, respectively as compared to the cylinder inclusion. Although there is no significant difference regarding the bandgap width in the 2nd bandgap, the shape of the inclusion could influence the 1st region of the bandgap which is the dominant frequency region of the blast loading, therefore is more critical to blast loading mitigation of the meta-panel.

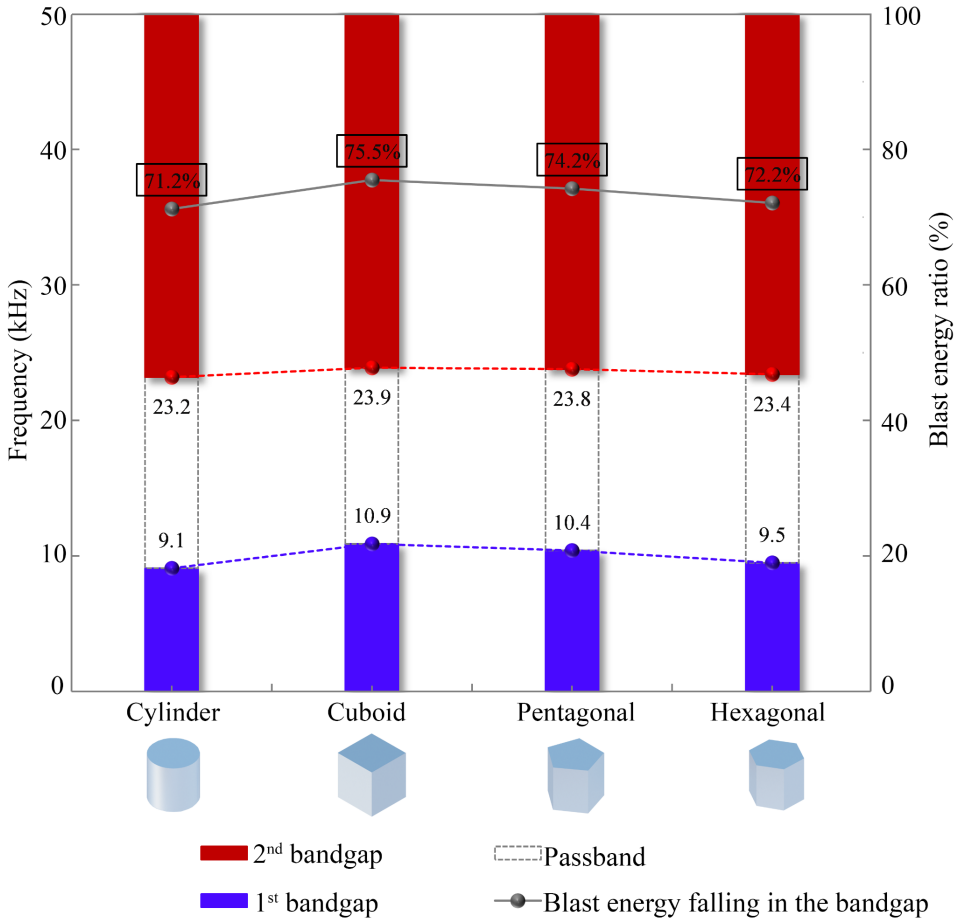


Fig. 24. Frequency band structures of the meta-truss bar with different inclusion shapes to show the proportion of blast energy falling into their bandgaps including the bandgap frequency on the left-hand side and the fractional blast energy on the right-hand side. Shaded areas in blue and red respectively indicate the bandgaps associated with the 1st and 2nd bandgaps while the passband is denoted by the dotted line. The boxed number indicates the proportion of blast energy falling into the bandgap (For interpretation of the references to colour in this figure legend, readers are referred to the web version of this article).

Fig. 25 presents the blast energy percentage in the passband of the meta-truss bar with the considered inclusion shapes. The blast loading energy in the passband of the meta-truss bar can be calculated by the area enclosed by the FFT spectrum of the blast loading in the passband as illustrated in Fig. 25. As shown in Fig. 24, the highest percentage of blast energy falling into

476 the bandgap of the meta-truss bar with cuboid shape core is 75.5%, because the meta-truss bar
477 with cuboid shape cores has the widest 1st bandgap. The maximum passband corresponds to the
478 inclusion with cylindrical shape and the blast loading energy fall in this passband is 28.8%,
479 followed by 27.9% and 25.5% for the pentagonal and hexagonal shapes, respectively. The truss
480 bar with the cuboid cores has the least percentage of blast energy transmission of 24.5%.

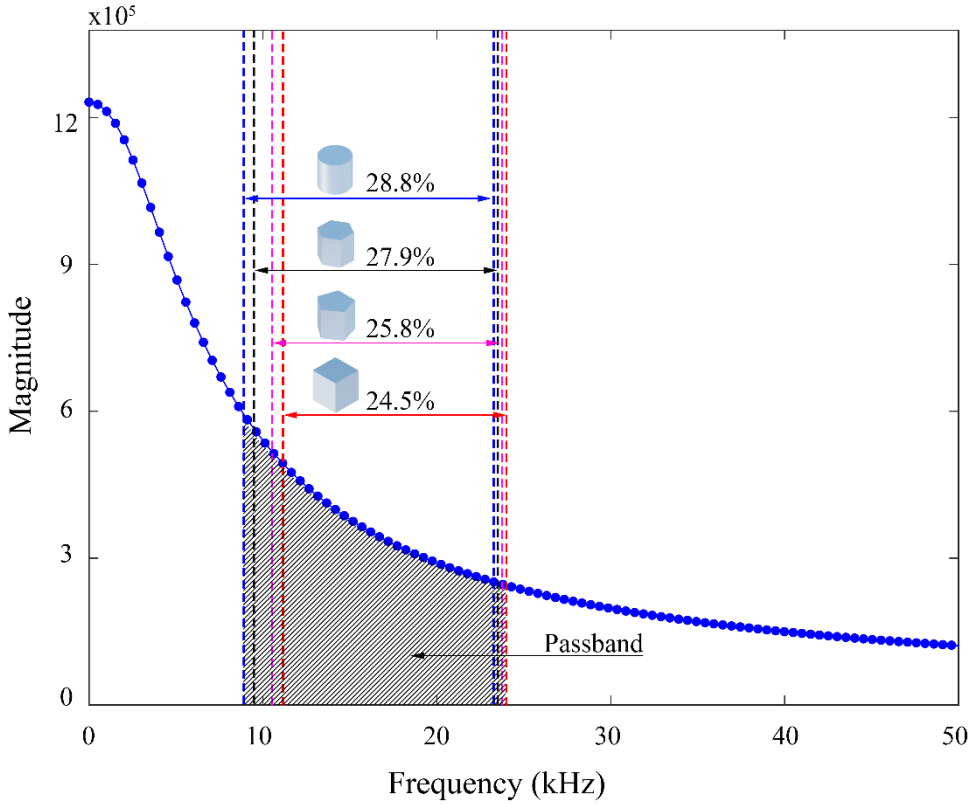


Fig. 25. Effect of inclusion shape on blast energy percentage in the passband of the meta-truss bar. The shaded area indicates the passband of the meta-truss while the dotted line denotes the upper bound of the 1st bandgap and lower bound of the 2nd bandgap. The red dashed line represents the cuboid resonator, followed by the magenta, the black, the blue for pentagonal prism, hexagonal prism and cylinder resonator, respectively (For interpretation of the references to colour in this figure legend, readers are referred to the web version of this article).

As expected, it can be observed from Fig. 26 that the meta-panel with cuboid inclusion shows a reduction in the central displacement of the back face-sheet and reaction force compared to the panels with other meta-truss bars. The varying inclusion geometries effectively affect the bandgaps, especially the 1$^{st}$ bandgap which covers the dominant frequency band of the blast loading, leading to the enhanced performance of the meta-panel. Consequently, the total energy absorption of the meta-panel with cuboid inclusion is the highest (i.e. 296 J) while the smallest energy absorption is associated with the meta-truss bar with cylindrical cores as shown in Fig. 27. It is worth noting that the energy absorption of other components including the front face-sheet and the outer tube is similar among all the considered panels due to the same stiffness. The back face-sheet of the panel with cylindrical inclusion experiences the largest deformation, implying higher energy absorption of the back face-sheet compared to other considered cases. As expected, the meta-core with the cuboid inclusion absorbs the most amount of energy, in which the most energy is the combination of the kinetic energy of the core and the internal energy of the coating. The least amount of energy absorption by the coatings and the cores corresponds to the cylindrical case, which is 80 J, followed by 85 J, and 90 J respectively for the hexagonal, and pentagonal cases. The best mitigation effectiveness of the meta-panels with cuboid resonators over the other resonator shapes is expected due to the smallest percentage of blast energy falling in its passband, as shown in Fig. 25. For a typical blasting wave, as shown in the FFT spectrum, the energy associated with the low-frequency range is significantly greater than that in the high-frequency range. Thus, though the resonator shape does not significantly affect the bandgap in the high-frequency range, it enhances the dynamic performance of the meta-panel by attenuating more energy falling in the low-frequency range. Particularly, the meta-truss bar with the cuboid resonator has the widest first bandgap among all the considered resonator shapes, indicating its best performance in resisting blast loading.

In general, the transient responses of the meta-panel significantly rely on the band structures of the meta-truss bar which are affected by the geometry of the inclusion. Although the cuboid shape exhibits better performances, due to the complex fabrication process and aligning with the cylindrical shape of the truss bar, the inclusion of cylindrical shape is recommended for practical application.

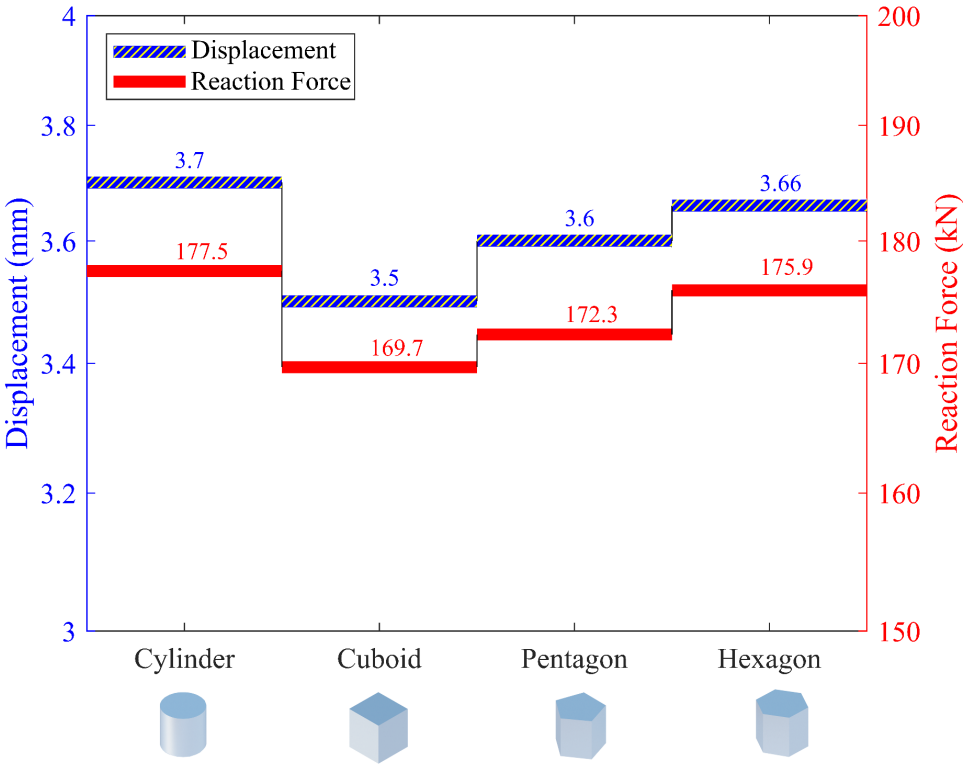


Fig. 26. Comparison of displacements and reaction forces between four meta-panels with different inclusion shapes under blast loading. The shaded areas in blue represent the displacement on the right-hand side while the reaction force is indicated by the red shaded areas on the right-hand side (For interpretation of the references to colour in this figure legend, readers are referred to the web version of this article).

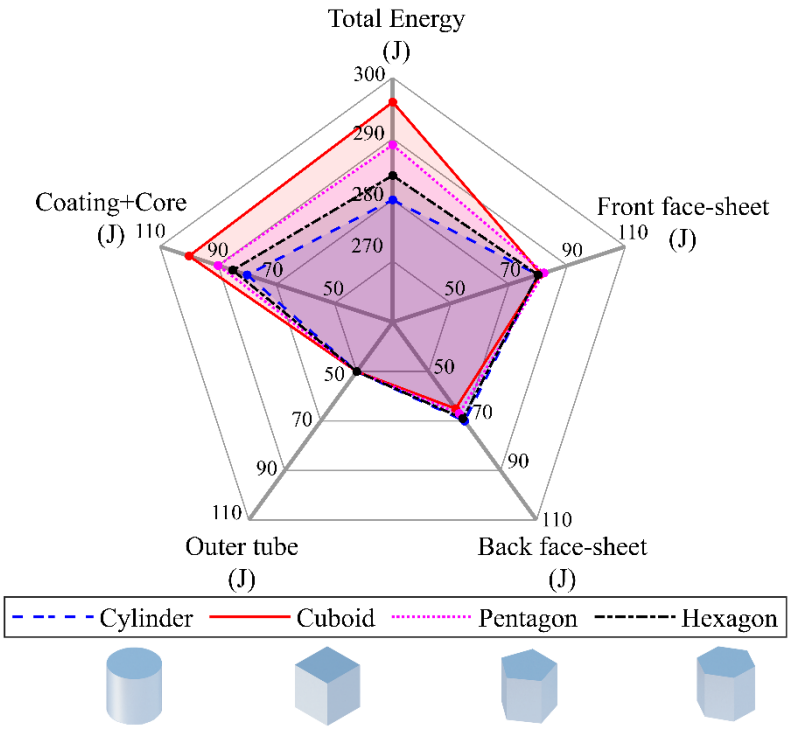


Fig. 27. Comparison of energy absorption of the meta-panel embedded with various inclusion shapes under blast loading. The red solid line represents the cuboid resonator, followed by the magenta dotted line, the black dash-dotted line, the blue dashed line for pentagonal prism, hexagonal prism and cylinder resonator, respectively (For interpretation of the references to colour in this figure legend, readers are referred to the web version of this article).

## 6. Conclusions

In this study, the dynamic response of the proposed meta-panel is examined to demonstrate its enhanced blast resistance capacity as compared to the conventional meta-panel. Using non-uniform inclusions in the meta-truss bar composing of multiple types of resonators by changing core materials, sizes, and/or geometries significantly enhances the transient performance of the meta-panel. Therefore, an appropriate design of core arrangements of the meta-truss bar can lead to better wave propagation mitigation and hence structural protection. Also, the frequency

band structure of the meta-truss core depends on the shape of inclusion and the cuboid inclusion is found to have the widest bandgaps among the four shapes considered in this study, therefore the meta-panel with cuboid resonator performs the best in blast loading effect mitigation. However, the inclusion of a cylindrical shape is recommended for practical application due to its easy fabrication. The results obtained in this study demonstrate the possibility of properly adjusting the materials, sizes, and geometries of resonator cores in the meta-truss bar to achieve the desired bandgaps for effective wave propagation mitigation, hence better structural protection performance of the meta-panel.

## Acknowledgments

The authors would like to acknowledge the financial support from the Australian Research Council via Laureate Fellowships FL180100196. The first author also acknowledges the support through the Australian Government Research Training Program Scholarship (RTP).

## References

[1] S. Palanivelu, W. van Paepegem, J. Degrieck, B. Reymen, E. Segers, J.M. Ndambi, J. Vantomme, J. Van Ackeren, J. Wastiels, D. Kakogiannis, D. Van Hemelrijck, Performance of Sacrificial Cladding Structure Made of Empty Recyclable Metal Beverage Cans under Large-Scale Air Blast Load, Applied Mechanics and Materials, 82 (2011) 416-421.
[2] J. Liu, W. Chen, H. Hao, Z. Wang, Numerical study of low-speed impact response of sandwich panel with tube filled honeycomb core, Compos. Struct., 220 (2019) 736-748.
[3] W. Van Paepegem, S. Palanivelu, J. Degrieck, J. Vantomme, B. Reymen, D. Kakogiannis, D. Van Hemelrijck, J. Wastiels, Blast performance of a sacrificial cladding with composite tubes for protection of civil engineering structures, Compos Part B: Eng, 65 (2014) 131-146.
[4] N.S. Choudhary, M.D. Goel, S. Panchal, Numerical Analysis of Innovative Sacrificial Protection System under Blast Loading, Practice Periodical on Structural Design and Construction, 27 (2022) 04021075.
[5] Z. Li, W. Chen, H. Hao, Blast mitigation performance of cladding using square dome-shape kirigami folded structure as core, Int J Mech Sci, 145 (2018) 83-95.
[6] X. Yang, J. Ma, Y. Shi, Y. Sun, J. Yang, Crashworthiness investigation of the bio-inspired bi-directionally corrugated core sandwich panel under quasi-static crushing load, Mater. Des., 135 (2017) 275-290.
[7] N.S. Ha, G. Lu, Thin-walled corrugated structures: A review of crashworthiness designs and energy absorption characteristics, Thin-Walled Structures, 157 (2020) 106995.
[8] N.S. Ha, G. Lu, X. Xiang, Energy absorption of a bio-inspired honeycomb sandwich panel, J. Mater. Sci., 54 (2019) 6286-6300.

[9] T.N.T. Cao, V.H. Luong, H.N. Vo, X.V. Nguyen, V.N. Bui, M.T. Tran, K.K. Ang, A Moving Element Method for the Dynamic Analysis of Composite Plate Resting on a Pasternak Foundation Subjected to a Moving Load, International Journal of Computational Methods, 16 (2018) 1850124.
[10] S. Yao, H. Zhu, M. Liu, Z. Li, P. Xu, Energy absorption of origami tubes with polygonal cross-sections, Thin-Walled Structures, 157 (2020) 107013.
[11] J. Liu, Y. Li, X. Shi, W. Wang, Dynamic Response of Bird Strike on Aluminum Honeycomb-Based Sandwich Panels, Journal of Aerospace Engineering, 27 (2014) 520-528.
[12] S. Cheng, B. Xiao, X. Zhao, Y. Xin, H. Li, Drop-weight impact test on an integrated composite sandwich panel of aluminum honeycomb and epoxy resin, J. Mater. Res., 32 (2017) 2258-2265.
[13] X.-k. Lan, Q. Huang, T. Zhou, S.-s. Feng, Optimal design of a novel cylindrical sandwich panel with double arrow auxetic core under air blast loading, Defence Technology, 16 (2020) 617-626.
[14] G. Imbalzano, P. Tran, T.D. Ngo, P.V.S. Lee, A numerical study of auxetic composite panels under blast loadings, Compos. Struct., 135 (2016) 339-352.
[15] C.-C. Liang, M.-F. Yang, P.-W. Wu, Optimum design of metallic corrugated core sandwich panels subjected to blast loads, Ocean Engineering, 28 (2001) 825-861.
[16] X. Li, Z. Wang, F. Zhu, G. Wu, L. Zhao, Response of aluminium corrugated sandwich panels under air blast loadings: Experiment and numerical simulation, Int J Impact Eng, 65 (2014) 79-88.
[17] T.V. Le, A. Ghazlan, T. Ngo, T. Nguyen, Performance of a bio-mimetic 3D printed conch-like structure under quasi-static loading, Compos. Struct., 246 (2020) 112433.
[18] T.V. Le, A. Ghazlan, T. Ngo, T. Nguyen, A. Remennikov, A comprehensive review of selected biological armor systems – From structure-function to bio-mimetic techniques, Compos. Struct., 225 (2019) 111172.
[19] N.S. Ha, G. Lu, D. Shu, T.X. Yu, Mechanical properties and energy absorption characteristics of tropical fruit durian (Durio zibethinus), Journal of the Mechanical Behavior of Biomedical Materials, 104 (2020) 103603.
[20] L. Zhang, Z. Bai, F. Bai, Crashworthiness design for bio-inspired multi-cell tubes with quadrilateral, hexagonal and octagonal sections, Thin-Walled Structures, 122 (2018) 42-51.
[21] N.S. Ha, G. Lu, A review of recent research on bio-inspired structures and materials for energy absorption applications, Compos Part B: Eng, 181 (2020) 107496.
[22] N.S. Ha, T.M. Pham, W. Chen, H. Hao, G. Lu, Crashworthiness analysis of bio-inspired fractal tree-like multi-cell circular tubes under axial crushing, Thin-Walled Structures, 169 (2021) 108315.
[23] N.S. Ha, T.M. Pham, H. Hao, G. Lu, Energy absorption characteristics of bio-inspired hierarchical multi-cell square tubes under axial crushing, Int J Mech Sci, 201 (2021) 106464.
[24] F.W. Zok, S.A. Waltner, Z. Wei, H.J. Rathbun, R.M. McMeeking, A.G. Evans, A protocol for characterizing the structural performance of metallic sandwich panels: application to pyramidal truss cores, International Journal of Solids and Structures, 41 (2004) 6249-6271.
[25] L. Jing, L. Zhao, Blast resistance and energy absorption of sandwich panels with layered gradient metallic foam cores, J. Sandw. Struct. Mater., 21 (2017) 464-482.
[26] X. Ren, J. Shen, A. Ghaedizadeh, H. Tian, Y. Min Xie, Experiments and parametric studies on 3D metallic auxetic metamaterials with tuneable mechanical properties, Smart Mater. Struct., 24 (2015) 095016.
[27] X. Xiang, S. Zou, N.S. Ha, G. Lu, I. Kong, Energy absorption of bio-inspired multi-layered graded foam-filled structures under axial crushing, Compos Part B: Eng, 198 (2020) 108216.

[28] Z. Li, W. Chen, H. Hao, Dynamic crushing and energy absorption of foam filled multi-layer folded structures: Experimental and numerical study, Int J Impact Eng, 133 (2019) 103341.
[29] Z. Li, W. Chen, H. Hao, Numerical study of blast mitigation performance of folded structure with foam infill, Structures, 20 (2019) 581-593.
[30] D.T. Queheillalt, H.N.G. Wadley, Cellular metal lattices with hollow trusses, Acta Mater., 53 (2005) 303-313.
[31] X. Cao, H. Hua, Acoustic responses of the composite sandwich plates with lattice truss core to the subsonic turbulent boundary layer, Compos. Struct., 153 (2016) 176-192.
[32] S. Yin, L. Wu, L. Ma, S. Nutt, Pyramidal lattice sandwich structures with hollow composite trusses, Compos. Struct., 93 (2011) 3104-3111.
[33] G. Qi, L. Ma, Experimental investigation of composite pyramidal truss core sandwich panels with lightweight inserts, Compos. Struct., 187 (2018) 336-343.
[34] E.C. Clough, J. Ensberg, Z.C. Eckel, C.J. Ro, T.A. Schaedler, Mechanical performance of hollow tetrahedral truss cores, International Journal of Solids and Structures, 91 (2016) 115-126.
[35] J.-H. Lim, K.-J. Kang, Mechanical behavior of sandwich panels with tetrahedral and Kagome truss cores fabricated from wires, International Journal of Solids and Structures, 43 (2006) 5228-5246.
[36] U.K. Vaidya, M.V. Hosur, D. Earl, S. Jeelani, Impact response of integrated hollow core sandwich composite panels, Composites Part A: Applied Science and Manufacturing, 31 (2000) 761-772.
[37] X. Liu, X. Tian, T.J. Lu, D. Zhou, B. Liang, Blast resistance of sandwich-walled hollow cylinders with graded metallic foam cores, Compos. Struct., 94 (2012) 2485-2493.
[38] I. Elnasri, H. Zhao, Impact Response of Sacrificial Cladding Structure with an Alporas Aluminum Foam Core Under Blast Loading, International Journal of Applied Mechanics, 12 (2020) 2050094.
[39] H.B. Rebelo, C. Cismasiu, Robustness assessment of a deterministically designed sacrificial cladding for structural protection, Eng. Struct., 240 (2021) 112279.
[40] N.H. Vo, T.M. Pham, K. Bi, H. Hao, Model for analytical investigation on meta-lattice truss for low-frequency spatial wave manipulation, Wave Motion, 103 (2021) 102735.
[41] X. Xiang, Z. Fu, S. Zhang, G. Lu, N.S. Ha, Y. Liang, X. Zhang, The mechanical characteristics of graded Miura-ori metamaterials, Mater. Des., 211 (2021) 110173.
[42] N.H. Vo, T.M. Pham, K. Bi, W. Chen, H. Hao, Stress Wave Mitigation Properties of Dual-meta Panels against Blast Loads, Int J Impact Eng, 154 (2021) 103877.
[43] B. Li, Y. Liu, K.-T. Tan, A novel meta-lattice sandwich structure for dynamic load mitigation, J. Sandw. Struct. Mater., (2017) 1099636217727144.
[44] Z. Liu, C.T. Chan, P. Sheng, A.L. Goertzen, J.H. Page, Elastic wave scattering by periodic structures of spherical objects: Theory and experiment, Physical Review B, 62 (2000) 2446-2457.
[45] L. D'Alessandro, A.O. Krushynska, R. Ardito, N.M. Pugno, A. Corigliano, A design strategy to match the band gap of periodic and aperiodic metamaterials, Sci. Rep., 10 (2020) 16403.
[46] K.T. Tan, H.H. Huang, C.T. Sun, Blast-wave impact mitigation using negative effective mass density concept of elastic metamaterials, Int J Impact Eng, 64 (2014) 20-29.
[47] X. An, F. Sun, P. Yu, H. Fan, S. He, D. Fang, Negative Effective Mass Density of One-Dimensional Hierarchical Metacomposite, Journal of Applied Mechanics, 82 (2015).
[48] B. Li, K.T. Tan, Asymmetric wave transmission in a diatomic acoustic/elastic metamaterial, J. Appl. Phys., 120 (2016) 075103.

[49] Y. Liu, X. Su, C.T. Sun, Broadband elastic metamaterial with single negativity by mimicking lattice systems, J. Mech. Phys. Solids., 74 (2015) 158-174.
[50] C. Xu, W. Chen, H. Hao, H. Jin, Effect of engineered aggregate configuration and design on stress wave attenuation of metaconcrete rod structure, International Journal of Solids and Structures, (2021) 111182.
[51] M.H. Khan, B. Li, K.T. Tan, Impact load wave transmission in elastic metamaterials, Int J Impact Eng, 118 (2018) 50-59.
[52] X. Chen, Q. Ji, J. Wei, H. Tan, J. Yu, P. Zhang, V. Laude, M. Kadic, Light-weight shell-lattice metamaterials for mechanical shock absorption, Int J Mech Sci, 169 (2020) 105288.
[53] Z.-Y. Li, T.-X. Ma, Y.-Z. Wang, F.-M. Li, C. Zhang, Vibration isolation by novel meta-design of pyramid-core lattice sandwich structures, J. Sound. Vib., 480 (2020) 115377.
[54] R. Zhu, X.N. Liu, G.K. Hu, C.T. Sun, G.L. Huang, A chiral elastic metamaterial beam for broadband vibration suppression, J. Sound. Vib., 333 (2014) 2759-2773.
[55] Z. Lu, X. Yu, S.-K. Lau, B.C. Khoo, F. Cui, Membrane-type acoustic metamaterial with eccentric masses for broadband sound isolation, Appl. Acoust., 157 (2020) 107003.
[56] G. Finocchio, O. Casablanca, G. Ricciardi, U. Alibrandi, F. Garescì, M. Chiappini, B. Azzerboni, Seismic metamaterials based on isochronous mechanical oscillators, Appl. Phys. Lett., 104 (2014) 191903.
[57] Y. Zeng, Y. Xu, H. Yang, M. Muzamil, R. Xu, K. Deng, P. Peng, Q. Du, A Matryoshka-like seismic metamaterial with wide band-gap characteristics, International Journal of Solids and Structures, 185-186 (2020) 334-341.
[58] Z. Liu, X. Zhang, Y. Mao, Y.Y. Zhu, Z. Yang, C.T. Chan, P. Sheng, Locally Resonant Sonic Materials, Science, 289 (2000) 1734.
[59] S. Alamri, B. Li, G. McHugh, N. Garafolo, K.T. Tan, Dissipative diatomic acoustic metamaterials for broadband asymmetric elastic-wave transmission, J. Sound. Vib., 451 (2019) 120-137.
[60] N.H. Vo, T. Pham, K. Bi, H. Hao, Impact Load Mitigation of Meta-panels with Single Local Resonator Meta-truss core, Eng. Struct., Under Review (2021).
[61] P.A. Shirbhate, M.D. Goel, A Critical Review of Blast Wave Parameters and Approaches for Blast Load Mitigation, Archives of Computational Methods in Engineering, (2020).
[62] G. Imbalzano, S. Linforth, T.D. Ngo, P.V.S. Lee, P. Tran, Blast resistance of auxetic and honeycomb sandwich panels: Comparisons and parametric designs, Compos. Struct., 183 (2018) 242-261.
[63] W. Chen, H. Hao, Numerical study of blast-resistant sandwich panels with rotational friction dampers, Int. J. Struct. Stab. Dyn., 13 (2013).
[64] C.-Y. Lee, M.J. Leamy, J.H. Nadler, Frequency band structure and absorption predictions for multi-periodic acoustic composites, J. Sound. Vib., 329 (2010) 1809-1822.
[65] H. Yasuda, J.J.J.-I.A.f.S. Yang, S. Structures, Tunable Frequency Band Structure of Origami-Based Mechanical Metamaterials, 58 (2017) 287-294.
[66] C. Comi, L. Driemeier, Wave propagation in cellular locally resonant metamaterials, Lat. Am. J. Solid. Struct., 15 (2018).
[67] C. Xu, W. Chen, H. Hao, The influence of design parameters of engineered aggregate in metaconcrete on bandgap region, J. Mech. Phys. Solids., 139 (2020) 103929.
[68] P.R. Villeneuve, M. Piché, Photonic band gaps in two-dimensional square lattices: Square and circular rods, Phys Rev B Condens Matter, 46 (1992) 4973-4975.
[69] A.O. Krushynska, V.G. Kouznetsova, M.G.D. Geers, Towards optimal design of locally resonant acoustic metamaterials, J. Mech. Phys. Solids., 71 (2014) 179-196.
[70] N.T. Lam, I. Howard, L. Cui, Path planning for the Platonic solids on prescribed grids by edge-rolling, PLOS ONE, 16 (2021) e0252613.

[71] N.T. Lam, I. Howard, L. Cui, A Literature Review on Path Planning of Polyhedrons with Rolling Contact, in: 2019 4th International Conference on Control, Robotics and Cybernetics (CRC), 2019, pp. 145-151.

## List of Figures

Fig. 10. Analytical transmission coefficient profile of two zones of the meta-truss bar incorporating two types of resonators (Aluminium and Tungsten). The passband $PB_2$ falls into the low bandgap of Zone 1 ($LB_1$), while the high bandgap of Zone 2 ($HB_2$) covers the passbands of zone 1 ($PB_1$). The complete bandgap is formed by combining all the four bandgaps.

Fig. 11. Displacement-time history at three points, i.e. the input point (A), the middle point (B), and the output point (C) in the meta-truss bar with two types of resonators. A prescribed displacement excitation is applied at one end of the meta-truss bar (A), the output displacements at the middle point (B) and the ending point (C) are presented to prove the mitigation effectiveness.

Fig. 12. FFT spectrum of displacement at the three points, i.e. the input point (A), the middle point (B), and the output point (C) in the meta-truss bar with two types of resonators. A prescribed displacement excitation is put at one end of the meta-truss bar (A), the output displacements at the middle point (B) and the ending point (C) are captured and transformed to the frequency domain.

Fig. 13. Scalograms of displacement in the time-frequency domain at different points (a) point A, (b) point B, and (c) point C. A prescribed displacement excitation is put at one end of the meta-truss bar (A), the output displacements at the middle point (B) and the ending point (C) are captured and transformed to the time-frequency domain using CWT.

Fig. 14. Diagrams showing deformed meta-panel subjected to blast loading and the deformation on the central symmetric plane of the bottom face-sheet of three meta-panels with different meta-truss bar configurations (a) Aluminium and Tungsten resonator meta-panel and (b-c) are uniform resonator meta-panels made of tungsten and aluminium, respectively.

Fig. 15. Comparison of reaction force-time history curves between the three meta-panels including meta-panel with two types of resonators and conventional meta-panels with uniform resonators (Al or W) under blast loading.

Fig. 16. Comparison of energy absorptions of different parts of the three meta-panels including meta-panel with two types of resonators and conventional meta-panel with uniform resonator (Al or W) under blast loading.

Fig. 17. Schematic diagram of meta-truss bars with different sizes of resonators (a) non-uniform resonator meta-truss bar with two sizes of resonators and (b-c) are uniform resonators meta-truss bar with the core radius of 7 mm and 4 mm, respectively.

Fig. 18. Analytical transmission coefficient profile of two zones of the meta-truss bar with two types of resonators with the radii of 7 mm and 4 mm. The passband $PB_2$ falls into the low

765 bandgap of Zone 1 ($LB_1$), while the high bandgap of Zone 2 ($HB_2$) covers the passband of zone
766 1 ($PB_1$). The complete bandgap is formed by combining all the bandgaps.
767 Fig. 19. Displacement-time history at the three points, i.e. the input point (A), the middle point
768 (B), and the output point (C) in the meta-truss bar with two resonator sizes. A prescribed
769 displacement excitation is applied at one end of the meta-truss bar (A), the output displacements
770 at the middle point (B) and the ending point (C) are presented to prove the mitigation
771 effectiveness.
772 Fig. 20. FFT spectrum of displacement at the three points, i.e. the input point (A), the middle
773 point (B), and the output point (C) in the meta-truss bar with two resonator sizes. A prescribed
774 displacement excitation is applied at one end of the meta-truss bar (A), the output displacements
775 at the middle point (B) and the ending point (C) are captured and transformed to the frequency
776 domain.
777 Fig. 21. Scalograms for displacement in the time-frequency domain at different points (a) point
778 A, (b) point B, and (c) point C. A prescribed displacement excitation is applied at one end of
779 the meta-truss bar (A), the output displacements at the middle point (B) and the ending point
780 (C) are captured and transformed to the time-frequency domain using CWT.
781 Fig. 22. Comparison of displacement-time history curves of the back face-sheet between the
782 three meta-panels including meta-panel with two resonator sizes and conventional meta-panels
783 with uniform resonators (7 mm or 4 mm of radius) under blast loading.
784 Fig. 23. Representation and dimensions of meta-unit cells with various inclusion shapes
785 including (a) cylinder, (b) cuboid, (c) pentagonal prism, and (d) hexagonal prism.
786 Fig. 24. Frequency band structures of the meta-truss bar with different inclusion shapes to show
787 the proportion of blast energy falling into their bandgaps including the bandgap frequency on
788 the left-hand side and the fractional blast energy on the right-hand side. Shaded areas in blue
789 and red respectively indicate the bandgaps associated with the $1^{st}$ and $2^{nd}$ bandgaps while the
790 passband is denoted by the dotted line. The boxed number indicates the proportion of blast
791 energy falling into the bandgap (For interpretation of the references to colour in this figure
792 legend, readers are referred to the web version of this article).
793 Fig. 25. Effect of inclusion shape on blast energy percentage in the passband of the meta-truss
794 bar. The shaded area indicates the passband of the meta-truss while the dotted line denotes the
795 upper bound of the $1^{st}$ bandgap and lower bound of the $2^{nd}$ bandgap. The red dashed line
796 represents the cuboid resonator, followed by the magenta, the black, the blue for pentagonal
797 prism, hexagonal prism and cylinder resonator, respectively (For interpretation of the references
798 to colour in this figure legend, readers are referred to the web version of this article).

Fig. 26. Comparison of displacements and reaction forces between four meta-panels with different inclusion shapes under blast loading. The shaded areas in blue represent the displacement on the right-hand side while the reaction force is indicated by the red shaded areas on the right-hand side (For interpretation of the references to colour in this figure legend, readers are referred to the web version of this article).

Fig. 27. Comparison of energy absorption of the meta-panel embedded with various inclusion shapes under blast loading. The red solid line represents the cuboid resonator, followed by the magenta dotted line, the black dash-dotted line, the blue dashed line for pentagonal prism, hexagonal prism and cylinder resonator, respectively (For interpretation of the references to colour in this figure legend, readers are referred to the web version of this article).

## List of Tables